Spatiotemporal Drivers of Hydrochemical Variability in a Tropical Glacierized Watershed in the Andes

Leila Saberi[1], Gene-Hua Crystal Ng[2], Leah Nelson[1], Wei Zhi[3], Li li[3], Jeff La Frenierre[4], and Morgan Johnstone[1]

[1]University of Minnesota
[2]University of Minnesota - Twin Cities
[3]Pennsylvania State University
[4]Gustavus Adophys College

November 23, 2022

Abstract

Little is currently known about the hydrochemistry of tropical glacierized mountain watersheds, which are among the most vulnerable systems in the world. Glacier retreat may impact their export of nutrients, with possible implications for downstream ecosystems. Solute export depends on dynamic and heterogeneous processes within the watershed, which calls for investigations of the different factors controlling hydrochemical variability. To examine these in a sub-humid glacierized watershed in Ecuador, we implemented a hydrological model that incorporates reactive transport, RT-Flux-PIHM. Our results demonstrate that calibrating the model to hydrochemical in addition to hydrological data is important for constraining groundwater fluxes, which we found to contribute 78% of stream discharge and to include 35% of the total glacial meltwater. Stream chemistry fluctuations are strongly controlled by varying contributions of groundwater, which contains high concentrations of reactive ions predominantly sourced from silicate mineral dissolution. The spatial variability in these concentrations, however, is driven more by heterogeneous evapotranspiration resulting from sharp montane vegetation gradients. With this concentrating effect, evapotranspiration also largely determines seasonal patterns in groundwater chemistry, with highest concentrations occurring in dry seasons, even when dissolution rates are low due to low soil moisture. While groundwater serves as a primary end-member source of streamwater, glacier melt-dominated surface runoff acts as a second source that imposes dilution events on an otherwise chemostatic concentration and discharge (C-Q) graph. Glacier melt overall decreases stream concentrations and increases discharge, with the latter effect dominating such that solute exports (C*Q) increase by 23% with melt.

Spatiotemporal Drivers of Hydrochemical Variability in a Tropical Glacierized Watershed in the Andes

Leila Saberi[1], G.-H. Crystal Ng[1,2], Leah Nelson[1], Wei Zhi[3], Li Li[3], Jeff La Frenierre[4], Morgan Johnstone[1]

[1]Department of Earth Sciences, University of Minnesota – Twin Cities, Minneapolis, MN 55455, USA
[2]Saint Anthony Falls Laboratory, University of Minnesota – Twin Cities, Minneapolis, MN 55414, USA
[3]Department of Civil & Environmental Engineering, Pennsylvania State University, University Park, PA 16802-1294, USA
[4]Department of Geography, Gustavus Adolphus College, St. Peter, MN 56082, USA

Key Points:

- Model calibration to hydrochemical data improves constraints on subsurface flowpaths and fluxes.
- Mineral dissolution controls mean solute quantities in the watershed, while evapotranspiration controls spatial and seasonal variability.
- Glacial meltwater enhances ion export via greater dissolution and flushing from subsurface.

Corresponding author: Leila Saberi, saber017@umn.edu

Abstract

Little is currently known about the hydrochemistry of tropical glacierized mountain watersheds, which are among the most vulnerable systems in the world. Glacier retreat may impact their export of nutrients, with possible implications for downstream ecosystems. Solute export depends on dynamic and heterogeneous processes within the watershed, which calls for investigations of the different factors controlling hydrochemical variability. To examine these in a sub-humid glacierized watershed in Ecuador, we implemented a hydrological model that incorporates reactive transport, RT-Flux-PIHM. Our results demonstrate that calibrating the model to hydrochemical in addition to hydrological data is important for constraining groundwater fluxes, which we found to contribute 78% of stream discharge and to include 35% of the total glacial meltwater. Stream chemistry fluctuations are strongly controlled by varying contributions of groundwater, which contains high concentrations of reactive ions predominantly sourced from silicate mineral dissolution. The spatial variability in these concentrations, however, is driven more by heterogeneous evapotranspiration resulting from sharp montane vegetation gradients. With this concentrating effect, evapotranspiration also largely determines seasonal patterns in groundwater chemistry, with highest concentrations occurring in dry seasons, even when dissolution rates are low due to low soil moisture. While groundwater serves as a primary end-member source of streamwater, glacier melt-dominated surface runoff acts as a second source that imposes dilution events on an otherwise chemostatic concentration and discharge (C-Q) graph. Glacier melt overall decreases stream concentrations and increases discharge, with the latter effect dominating such that solute exports (C*Q) increase by 23% with melt.

1 Introduction

Glacial meltwater in mountainous watersheds is an important source of water for communities living below them (Messerli et al., 2004; Kaser et al., 2010). Rising temperatures due to global warming results in increased rates of glacier retreat, raising concerns for regional water resource availability (Mark et al., 2017; Barnett et al., 2005). Growing evidence has shown that the rate of warming is highest in low latitudes and high altitudes. This includes tropical glacierized watersheds, more than 99% of which reside in the Andes (Bradley, 2006; Pepin et al., 2015). Tropical glacierized watersheds already experience year-round melt under present conditions (Kaser & Osmaston, 2002), and thus, they are highly vulnerable to on-going climate change and can be used as an early-indicator of climate change impacts on glacierized watersheds worldwide.

Much attention has been directed to the impact of glacier retreat in the Andes on streamflow (Barnett et al., 2005; Ostheimer et al., 2005; Bradley, 2006; Mark & Mckenzie, 2007; IPCC, 2007; Baraer et al., 2009; Saberi et al., 2019; Somers et al., 2019). In contrast, little attention has been paid to the potential hydrochemical impacts of glacier retreat. This represents a critical knowledge gap, because many tropical glacierized watersheds in the Andes likely undergo high weathering rates and serve as important sources of solutes to the Amazon basin. The majority of Andean glacierized mountains are located within the Andean volcanic belt (Stern, 2004) and are mainly composed of highly reactive silicate minerals (Stallard & Edmond, 1983; Ugolini et al., 2002; Torres et al., 2015). The weathering of silicate minerals increases significantly with high temperature and high moisture (Ugolini et al., 2002; White et al., 1998), conditions commonly found in humid tropical climates. Further, the weathering yield of minerals from combined physical and chemical processes has been noted worldwide to be greater in glacierized watersheds compared to non-glaciated catchments (Torres et al., 2017). While some weathered products form secondary minerals, most of them move into streams and are transported downgradient (Milner et al., 2017). Even though Andean glacierized mountains are located thousands of kilometers away from the Amazon river estuary and constitute only 13% of the Amazon basin, they are believed to be the main source of solutes that support ecological productivity in the basin, including sodium (Na^+), calcium (Ca^{2+}), and magnesium (Mg^{2+}) (Gibss, 1967; McClain & Naiman, 2008). However, this linkage between the Andes and Amazon may be threatened by environmental changes, and this impact on the Amazon Basin's ecological productivity is not well-understood. This calls for investigations into the hydrogeochemical function of tropical glacierized watersheds in order to understand their response to climate change and the corresponding ecological impacts.

Controls on the hydrochemistry of glacierized mountainous watersheds have been well-studied in temperate climates; these include meteorological drivers, geology, topography, and land-cover over different spatial and temporal scales (Devito et al., 2005; Williams et al., 2015; Engel et al., 2019). Meteorological conditions in particular have been found to have a significant influence on hydrochemical variability by increasing melt rates in temperate conditions (Milner et al., 2017). Temperature and radiation are the main driving forces for snow and ice melt (Sicart et al., 2008). Some previous studies in temperate glacierized watersheds found that solute concentrations are lower during high melt seasons due to the discharge of dilute meltwater into streams (Brown, 2002; Hindshaw et al., 2011; Kumar et al., 2019; Engel et al., 2019). However, other studies found that in-stream silica (SiO_2) [Anderson et al, 2005] and other major ion concentrations (Lewis et al., 2012; Stachnik et al., 2016) increase during high melt seasons mainly due to the increase in the hydrological connectivity of the catchment, which accelerates mineral dissolution. Bedrock and surficial geology also play an important role in controlling watershed hydrochemistry, both directly through geochemical input or immobilization of solutes (Tranter et al., 1996; Katsuyama et al., 2010) as well as indirectly through their physical influence on flow pathways (Farvolden, 1963; McGuire et al., 2005; Tetzlaff et al., 2009; Maher, 2011; Benettin et al., 2015).

Compared to temperate mountainous watersheds (Collins, 1999; Feng et al., 2012; Milner et al., 2009; Brighenti et al., 2019), relatively little is known about the factors controlling stream chemistry in tropical glacierized mountainous systems. Hydrochemical observations have mostly been used only as conservative tracers to determine relative meltwater contributions to stream discharge (Mark & Mckenzie, 2007; Baraer et al., 2009, 2015; Wilson et al., 2016; Minaya, 2016; Saberi et al., 2019). However, some recent studies have revealed dynamic and complex hydrochemical processes. Fortner et al. (2011) showed that glacier retreat in the Peruvian Cordillera Blanca is exposing sulfide-rich rock outcrops, leading to impaired water quality in streams. A set of hydrochemical studies spanning the Andes to Amazon transition included non-glacierized watersheds in the Peruvian Andes and showed that spatial heterogeneity among sub-catchments control temporal variations in stream discharge chemistry through dilution or weathering effects (Torres et al., 2015, 2017; Baronas et al., 2017). Together, these initial hydrochemical investigations in the tropical Andes point to the importance of understanding the role of spatiotemporal variability in driving the export of solutes.

Regardless of climate, many hydrochemical studies rely on stream concentration and discharge (C-Q) relationship analysis (Godsey et al., 2009). An advantage to this approach is its relative ease of implementation with a single surficial measurement point at the stream outlet. C-Q relationship analysis serves as an indirect way of inferring processes within the watershed that give rise to observed changes in concentration and discharge. However, because of the lack of explicit, fine-scale process examination in C-Q analysis, uncertainties persist when evaluating the individual roles of different hydrological and hydrochemical processes (Li et al., 2017). In particular, limitations in C-Q analysis for evaluating groundwater processes present a major weakness in many snow and ice-covered mountainous watersheds, because various hydrological studies have shown that in addition to melt runoff, groundwater can also contribute significantly to streamflow (Huth et al., 2004; Hood et al., 2006; Tague et al., 2008; Baraer et al., 2015; Andermann et al., 2012; Pohl et al., 2015; Engel et al., 2016; Harrington et al., 2018; Saberi et al., 2019; Somers et al., 2019). Some studies in non-glacierized tropical Andean watersheds have tackled the challenge of spatially lumped C-Q analysis by evaluating the sub-catchment C-Q relationships to show that varying sub-tributary discharge controls conditions at the outlet (Torres et al., 2015; Baronas et al., 2017). This approach nonetheless only looks explicitly at surface processes at different sub-catchments and can only offer indirect evidence for subsurface weathering and geochemical reactions (Torres et al., 2015; Baronas et al., 2017); in fact, the authors acknowledge that quantitative assessment of fluid transit and mineral contact times in the ground are precluded by data sparsity in the remote Andean sites (Torres et al., 2015).

A recently developed, spatially distributed and physically based model that integrates watershed hydrology and reactive transport, "RT-Flux-PIHM (Bao et al., 2017)", is now making it possible to directly evaluate spatiotemporal controls on the hydrochemistry within a watershed without exhaustive measurements (Li et al., 2017; Zhi et al., 2019). Previous applications of the model at two intensive study watersheds in the temperate U.S. (Susquehanna Shale Hills Critical Zone Observatory and Coal Creek in Crested Butte, CO) included an explicit representation of subsurface hydrochemistry, which led to quantitative insights into drivers of the degree of chemostasis in the watersheds. Results show strong seasonal controls through both hydrologic (effects of connectivity, solute flushing, and subsurface flow contributions) and geochemical (effect of mineral reactivity via wetted surfaces and dissolved organic carbon reactions) processes across the entire watershed (Li et al., 2017; Zhi et al., 2019; Wen et al., 2020). These early applications are paving the way for new questions, such as how other types of seasonal patterns (e.g., warmer and wetter tropical conditions with additional snow and ice melt contributions), lithologies (e.g., silicate-dominated volcanic soils underlain by fractured bedrock), and vegetation coverage (e.g., discrete vegetation line in high mountain watersheds) might support or counteract the tendency for chemostasis. In the tropical Andes, the degree of chemostasis and corresponding variations in nutrient export have important implications for critical downstream ecosystems as glaciers retreat.

In this study, we leverage RT-Flux-PIHM to answer two main questions in a sparsely instrumented glacierized watershed on Volcán Chimborazo in the tropical Ecuadorian Andes: (1) What is the role of hydrological and geochemical processes in controlling the spatiotemporal variability of concentrations of major ions in groundwater and streamwater? (2) What is the influence of glacial melt on hydrochemical variability in the watershed? The answer to the first question will provide general insights into vulnerable glacierized watersheds. Because we hypothesize that the influence of glacial melt will depend on its interactions with hydrogeological, ecohydrological, and weathering processes across the watershed, the answer to the first question will also help to address the second question.

2 Study Site Description

Volcán Chimborazo is a glacierized stratovolcano in Ecuador (Figure 1) that supplies water to over 200,000 people (INEC, 2010). Chimborazo experiences an inner tropical climate, characterized by minimal annual temperature variation (~2°C variability) and moderately seasonal precipitation with generally two wetter seasons (February-May and October-November) and two drier seasons that have less amounts of precipitation (Clapperton, 1990). Because of the Amazon Basin to the east (Vuille & Keimig, 2004; Smith et al., 2008), more humid conditions can be found on the northeast flank with more precipitation (2000 mm/yr) than the southwest (500 mm/yr) (Clapperton, 1990). El Niño and La Niña events cause variability in temperature and precipitation, with El Niño generally bringing drier and hotter conditions and La Niña wetter and cooler conditions throughout the Andes (Vuille & Bradley, 2000; Bradley et al., 2003; Wagnon et al., 2001; Francou, 2004; Vuille & Keimig, 2004; Smith et al., 2008). El Niño events have been found to potentially enhance glacier ablation (Francou, 2004; Favier, 2004; Vuille et al., 2008; Veettil et al., 2014). Within the June 2016-June 2017 time frame of this study, a strong El Niño event brought higher temperature and lower precipitation than normal to the watershed during November to February. Also during this year, wet conditions were observed over June to October (2015) and March to May (2016), which differ slightly from the general wet months noted above.

Temperatures have increased by 0.11°C /decade around Volcán Chimborazo since 1986 (Vuille et al., 2008; La Frenierre & Mark, 2017), which has been partly responsible for a 21% reduction in ice surface area from 1986-2013 and 180 m increase in the mean minimum elevation of clean ice (La Frenierre & Mark, 2017). Though instrumental data are ambiguous, community members indicate the local precipitation has decreased in recent decades (La Frenierre & Mark, 2017). This study focuses on the 7.5 km^2 Gavilan Machay sub-catchment on the sub-humid northeast flank of Chimborazo (Figure 1). Gavilan Machay has an altitude range of 3800 to 6400 m a.s.l and is 34% glacierized by the Reschreiter Glacier. Water from Gavilan Machay eventually reaches the Amazon below the confluence of Río Maranon, the principal upper tributary of the Amazon River, via the Río Mocha, Río Ambato, Río Chambo, and Río Pastaza. Gavilan Machay is of particular concern because it discharges into the Río Mocha channel immediately upstream of the Boca Toma diversion point (3895 m a.s.l. elevation) for the largest irrigation system on Volcán Chimborazo. Saberi et al. (2019) found that currently stream discharge from Gavilan Machay may contain up to 50% glacier meltwater, which has future implications for the downstream irrigation system as the glaciers continue to retreat.

Páramos – the biologically rich grasslands of the tropical Andes– are the most common ecosystem across the watershed below about 4600 m a.s.l. (Figure 2a). Ecologically, the páramo has high plant diversity (>5000 species), mainly consisting of tussock grasses, cushion plants, dwarf shrubs, ground

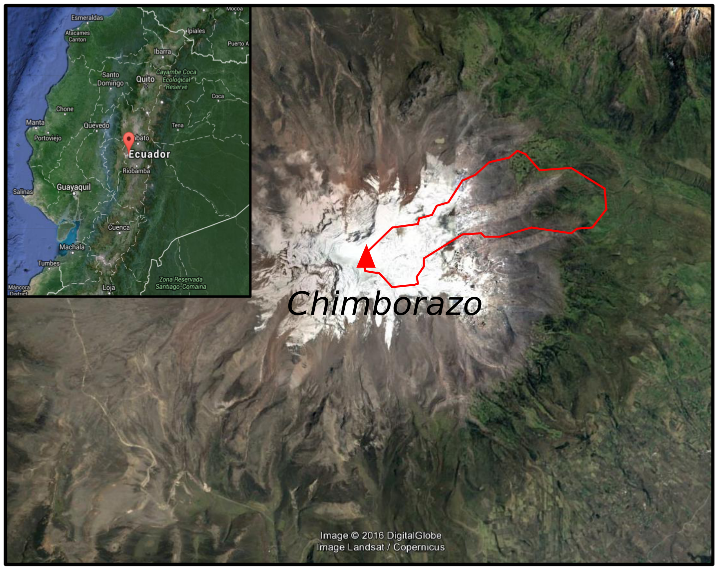

Figure 1: Satellite image of Volcán Chimborazo with the Gavilan Machay watershed outlined in red and its location in Ecuador shown in the inset map.

rosettes, and giant rosettes. Wet páramos are mainly composed of Andosol soils of volcanic origin and have high porosity and water retention capacity (Podwojewski et al., 2002; Buytaert et al., 2006; Buytaert & Beven, 2011; Minaya, 2016). The primary geology of Chimborazo consists of layered lava and pyroclastic flows, overlaid by thick ash deposits and vitric andosol (Figure 2b) (Barba et al., 2008; Samaniego et al., 2012). The morphology of the watershed has been influenced largely by glacial deposits and moraines from the Last Glacial maximum (LGM: 33-14 ka), the Late Glacial (LG: 13-15 ka), and the Neo-Glacial Period (NG: <5 ka). The presence of young volcanic fractured bedrock along with páramo soils and glacial deposits (Barba et al., 2005; Samaniego et al., 2012) facilitates water movement through the subsurface, which enhances both groundwater contribution to streamflow and weathering processes that release ions into the water (Stallard & Edmond, 1983). Previous hydrochemical observations in the Gavilan Machay watershed shows that the total dissolved solids concentrations in springs, proxies for groundwater, and streamflow increases as the elevation decreases (Saberi et al., 2019). This suggests that mineral reactions are releasing solutes into water as it flows downgradient in the watershed. Based on observations, sodium, calcium, and magnesium are the major ions present in the groundwater and surface water.

3 Geochemical Observations

3.1 Sites and Sampling Method

Three locations were selected for soil sampling along an elevation gradient (at 4510, 4240, and 3990 m a.s.l.) (Figure 2b). The highest elevation sample (S-1) was collected from moraine sediments, while the other two (S-2 and S-3) were taken near the stream channel (Figure 2b). A 3-inch diameter auger was used for soil profile sampling. At all sampling sites, shallow refusal was hit on buried cobbles and a single sample was collected from 3 and 5 cm depth. Two rock samples were collected at exposed outcrops, at 4950 m a.s.l. and 4000 m a.s.l. (R-1 and R-2, respectively, Figure 2b). The high elevation rock sample (R-1) was collected from Guano lava flows while the low elevation rock sample was collected from Holocene pyroclastic flow deposits (Barba et al., 2008). Details about the water sampling (locations in figure 2a) and analysis are in Saberi et al. (2019). Samples taken at spring sites were used to represent groundwater and will be referred to as "groundwater" to simplify the text.

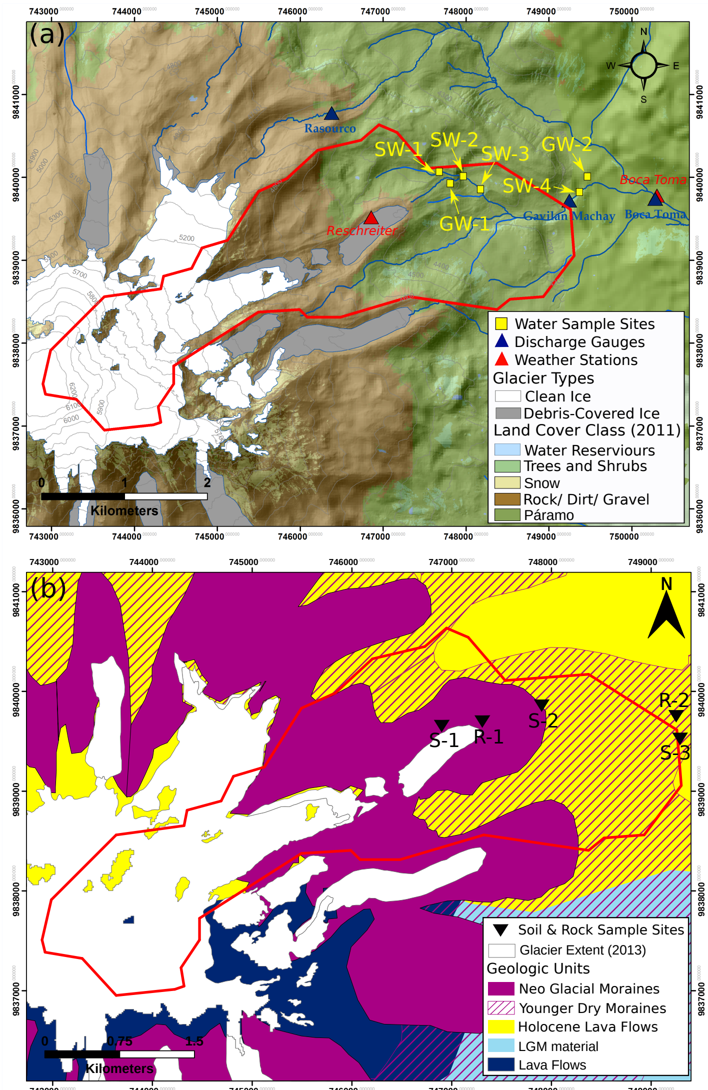

Figure 2: (a) Land cover and locations of monitoring stations and water sampling within the Gavilan Machay watershed. (b) Geologic map of Volcán Chimborazo and locations of soil and rock sampling within the Gavilan Machay watershed. The boundary of the Gavilan Machay watershed is outlined in red. Maps were adapted from McLaughlin (2017).

3.2 XRD Analysis and Results

Soil samples were air-dried and stored in resealable bags. Bulk soil and rock composition was determined using X-ray diffraction (XRD) analysis. Aggregate soils and rock were hand-ground to a fine powder. To separate the fine fraction from the aggregate sample, approximately 50g of each bulk soil sample was dry-sieved by hand. Organic matter was removed from the samples by the addition of a 3% hydrogen peroxide (H_2O_2) solution following Poppe et al. (2001) (USGS Open-File Report 01-041). Minerals in the bulk rock and soil samples were identified using XRD analysis. Samples were mounted on a glass slide using a smear technique to achieve random orientation. A Rigaku MiniFlex300 X-ray diffractometer was used to scan the samples from 5° to 65° 2θ at 30 kV voltage and 10mA current with Cr-Kα radiation. XRD patterns were analysed using the Jade software version 7.5.

Results from the XRD analysis indicate that the Gavilan Machay watershed is predominantly composed of aluminosilicate minerals including feldspar, pyroxene, and amphibole, which is consistent with most andosols worldwide (Shoji et al., 1994). Although the humid conditions in Gavilan Machay would generally be expected to promote high rates of chemical weathering, possibly producing clay minerals, the XRD results show no crystalline-clay minerals. Through grain size analysis, however, we found 8.5% and 18% of the bulk samples collected from 0-30 cm depth at 3800 m a.s.l. and 4500 m a.s.l., respectively, were clay- and silt-sized particles (smaller than 63 μm diameter). These estimates are consistent with previous soil studies on Chimborazo. Podwojewski et al. (2002) showed that shallow soil samples at 3800-4200 m a.s.l. on the drier northwestern flank of Chimborazo contain an average of 8.5% clay. Bartoli et al. (2007) found a slightly higher amount of 23% organo-mineral clay at 3800 m a.s.l. using a larger 2 mm diameter definition. It is likely the fine-grain fraction in our samples also contains organo-mineral clays that were resistant to our hydrogen peroxide treatment, as well as minerals with poor crystalline structure. Bartoli et al. (2007) characterized the Chimborazo's soils as aluandic andosols, which are regarded as non-allophanic andosol predominantly composed of aluminum complexed with organic matter (Takahashi & Shoji, 2002). The XRD analysis indicates that the bulk soil mineralogy is primarily dominated by that of the parent bedrock. As shown in Table 1, soil sample S-1 resembles the nearby rock sample R-1 (see map in Figure 2b) with three minerals in common from the feldspar and pyroxene mineral classes. Soil sample S-2 resembles rock sample R-2 based on similar feldspar minerals and proximity; soil sample S-3 likely originates from the R-2 rock sample, sharing minerals from both feldspar and pyroxene classes. Minerals from the amphibole class were present only in the R-1 rock sample and not in any soil samples, which suggests that they are relatively resistant to weathering compared to other classes. Even though the soil and rock properties have some differences, they are comprised of similar classes of minerals (feldspar and pyroxene) throughout the watershed. Relatively homogeneous soil characteristics have been observed elsewhere in the páramos of the Ecuadorian Andes, probably due to similar parent sources throughout an area (Buytaert et al., 2006). Different climatic conditions, however, can result in slight differences in soil properties (Buytaert et al., 2006; Podwojewski et al., 2002). Our findings indicate that the underlying bedrock geology is the major controller of soil mineralogy in the watershed, suggesting that the surficial sediment and deeper bedrock aquifers in the watershed may share similar hydrochemical signatures.

	Mineral	**Chemical Formula**	**R-1**	**S-1**	**R-2**	**S-2**	**S-3**
Feldspar	Albite	$Na(AlSi_3O_8)$			✓	✓	✓
	Anorthite	$Ca(Al_2Si_2O_8)$	✓	✓	✓		✓
	Andesine	$Na_{0.685}Ca_{0.347}Al_{1.46}Si_{2.54O8}$	✓	✓			
	Labradorite	$Na_{0.45}Ca_{0.55}Al_{1.5}Si_{2.5}O_8$		✓			
	Sanidine	$K(Si_3Al)O_8$	✓				✓
	Anorthoclase	$(Na_{0.75}K_{0.25})(AlSi_3O_8)$	✓		✓	✓	✓
Pyroxene	Enstatite ferroan	$Mg_{1.1}Fe_{0.87}Ca_{0.03}Si_2O_6$	✓	✓	✓		
	Diopside	$Ca(Mg,Al)(Si,Al)_2O_6$	✓		✓		✓
Amphibole	Arfvedsonite	$Na_3(Fe,Mg)_4FeSi_8O_{22}(F,OH)_2$	✓				
	Actinolite	$(Fe,Mg,Ca,Na,Mn)_7(Si,Al)_8O_{22}(OH)_{1.9}$	✓				

Table 1: Soil Mineralogy of Volcán Chimborazo. S-1, S-2, and S-3 are soil samples. R-1 and R-2 are rock samples from outcrops in the watershed. Sample locations are shown in Figure 2.

4 Model Description

4.1 RT-Flux-PIHM

Spatially distributed watershed models can integrate surface hydrology and groundwater flow through time and space to allow for the evaluation of their joint control on streamflow. Flux-PIHM (Shi et al., 2013) integrates land-surface and hydrologic simulations through a combination of two modules, the Noah land surface model (Noah-LSM) (Ek et al., 2003) and the PIHM hydrological model (Qu & Duffy, 2007). The multicomponent reactive transport module RT is an add-on to Flux-PIHM (Bao et al., 2017). The RT module takes calculated water fluxes and storage from Flux-PIHM (i.e. surface runoff, channel routing, infiltration, recharge, and subsurface lateral flow) and simulates hydrochemical processes including solute transport (advection, dispersion, and diffusion) and chemical reactions and outputs aqueous and solid phase geochemical concentrations. In addition to surface and subsurface water flow, evapotranspiration (ET) is simulated in the model as another key hydrologic flux that has a non-geochemical influence on solute concentrations. RT can simulate both equilibrium-controlled reactions including aqueous complexation, ion exchange, and surface complexation, and kinetically controlled reactions including mineral dissolution, precipitation, and redox reactions (Bao et al., 2017). Reactive transport is modeled in both the unsaturated and saturated zones. It is assumed that the surface runoff water has a very short interaction time with minerals and is not considered to undergo geochemical reactions in the RT module.

The rate of kinetically controlled mineral dissolution and precipitation is calculated using transition state theory (Helgeson et al., 1984; Lasaga, 1984):

$$R_m = A_{w,m} K_m (1 - \frac{IAP}{K_{eq}}) \tag{1}$$

where R_m is the dissolution/precipitation rate of the mineral m (mol/s), $A_{w,m}$ is the wetted surface area of the mineral m per volume of porous media (m^2/m^3), K_m is the intrinsic rate constant (mol/(m^2/s)), IAP is the ion activity product for the reaction, and K_{eq} is the thermodynamic equilibrium constant. The wetted surface area depends on groundwater storage through the following equation (Clow & Mast, 2010):

$$A_{w,m} = A_m S_w^n \tag{2}$$

where A_m is the total surface area of the mineral m per volume of the porous media under the fully saturated condition, S_w is the water saturation (m^3 water per m^3 pore space) and n is equal to 2/3 to represent the surface area to volume ratio of mineral grains (Mayer et al., 2002). The RT module and Flux-PIHM are coupled through the minerals' specific surface area (SSA) dependence on soil moisture.

The governing equation for reactive transport of an arbitrary solute m is as follows:

$$V_i \frac{d(S_{w,i}\theta_i C_{m,i})}{dt} = \sum_{j=N_{i,1}}^{N_{i,x}} (A_{ij} D_{ij} \frac{C_{m,j} - C_{m,i}}{I_{ij}} - q_{ij} C_{m,j}) + R_{m,i} \qquad m = 1, ..., np \tag{3}$$

where V_i is the total volume of grid cell i; $S_{w,i}$ is the water saturation (m^3 water per m^3 pore space), θ_i is the porosity (m^3 pore space per m^3 total volume); $C_{m,i}$ is the aqueous concentration of species m (mol/m^3 water); $N_{i,x}$ is the index of the neighboring elements of grid cell i, with the subscript x is set to two for unsaturated zone fluxes (infiltration and recharge) and four for saturated zone fluxes (recharge and lateral flow), respectively; A_{ij} is the interface area between the grid cell i and its neighbor cell j (m^2); D_{ij} is the dispersion/diffusion coefficient (m^2/s), I_{ij} is the distance between the center of the neighboring grid cells; q_{ij} is the volumetric flow rate across A_{ij} (m^3/s); and np is the total number of independent solutes.

In the model, a major assumption is that groundwater boundaries align with the surface watershed boundary, which prevents solutes from entering the watershed via groundwater. Another simplification is that in the model version used here, lateral "groundwater" flow represents the combination of shallow soil water interflow and groundwater flow. Further, all groundwater is eventually routed laterally into the stream and exits the watershed as surface discharge.

Full details about RT-Flux-PIHM can be found in Qu and Duffy (2007); Shi et al. (2013); Bao et al. (2017).

4.2 Model Setup

4.2.1 Hydrological and Transport Processes

The model simulations using RT-Flux-PIHM version 0.10.0 alpha were applied from June 2015 - June 2016. Implementation of the Gavilan Machay model domain and hydrological processes

follows Saberi et al's (2019) implementation of Flux-PIHM; a brief summary is provided here. To include ice melt in the simulation, a separate temperature-index module was added to the model. Glacial melt was estimated under the assumption that ablation occurs over the glacierized grid cells below the equilibrium line altitude (ELA) at 5050 m a.s.l (La Frenierre & Mark, 2014). The PIHMgis software (Bhatt et al., 2014) was used to discretize the domain into 188 triangular cells. Land-cover was set as grassland at the lowest elevations to represent páramo, barren/sparsely vegetated for the mid-altitude, and perennial ice/snow for the ice-covered areas (Figure 2a). Built-in land cover parameters from Noah-LSM were used for each land-cover type. Leaf area index for the vegetated parts of the watershed were from MODIS (Vermote, 2015).
In Saberi et al. (2019), soil hydraulic parameters of Flux-PIHM were calibrated to stream discharge measurements and hydrochemical mixing model estimates of melt contributions. In this study, using RT-Flux-PIHM, soil hydraulic parameters were directly constrained using major ion concentrations in the stream and groundwater, in addition to stream discharge (Table 4).

4.2.2 Geochemical Processes

The RT module was implemented with equilibrium aqueous complexation reactions for major elements (Na^+, Ca^{2+}, Mg^{2+}, chloride (Cl^-), and silica (SiO_2)) and pH, and with kinetic mineral reactions. Aqueous chemistry measurements were used to constrain mineral dissolution kinetic parameters. The chemical concentrations at the GW-1 and GW-2 spring (groundwater) sampling points (Fig 2a) were used to establish two different initial groundwater geochemical conditions for the spin-up run, one for the vegetated portion of the watershed and the other for the bare soil/ice-covered portion of the watershed (Table 2). The model was run in a spin-up mode until species reached a steady state such that their concentrations did not change with time. Due to the approximate nature of the spin-up, averaged steady-state concentrations of groundwater in the vegetated cells and in the bare soil/ice-covered cells were used as spatially uniform initial conditions for these respective portions of the watershed in the final simulation. As shown in Table 2, the measured and spun-up initial concentrations were higher at lower elevations (grassland) (Figure 2a). Although glacier melt samples had slightly higher concentrations than precipitation samples, they were of similar orders of magnitude that were much lower than that of the groundwater and streamwater samples. This justified the use of the same geochemical composition for both precipitation and glacial melt in the model in order to simplify the implementation with only one forcing condition for the two types of inputs. Precipitation and glacier melt concentrations were assumed to be constant over space and time.

	Precipitation	Glacial Melt	Grassland (Observed)	Grassland (Initial Condition)	Sparsely Vegetated and Ice-covered (observed)	Sparsely Vegetated and Ice-covered (initial condition)
Elemental Species (mol/l except for pH)						
pH	6.3	5.76	5.64	5.5	5.51	5.5
Na^+	2.78×10^{-5}	4.71×10^{-5}	2.41×10^{-4}	5.1×10^{-5}	1.94×10^{-4}	4.2×10^{-5}
Ca^{2+}	2.27×10^{-5}	3.36×10^{-5}	2.11×10^{-4}	2.1×10^{-5}	1.9×10^{-4}	2.11×10^{-5}
Mg^{2+}	1.43×10^{-6}	7.45×10^{-5}	2.59×10^{-4}	2.5×10^{-5}	1.8×10^{-4}	1.8×10^{-5}
Cl^-	3.77×10^{-5}	4.12×10^{-5}	9.04×10^{-5}	6.2×10^{-6}	5.81×10^{-5}	9.1×10^{-6}
SiO_2	0	0	2.54×10^{-4}	2.3×10^{-5}	2.93×10^{-4}	2.8×10^{-5}

Table 2: Initial chemical composition of groundwater, precipitation, and glacial melt in different portions of the Gavilan Machay watershed. The same chemical composition was applied to both bare soil and ice-covered areas. Precipitation concentrations were used for both glacial meltwater and precipitation in the simulations.

4.2.2.1 *Non-reactive Chloride Processes*

Due to the absence of chloride-containing minerals in the XRD results, we used Cl^- as a non-reactive tracer, which we assume enters the watershed through wet atmospheric deposition. The higher Cl^- concentrations in the groundwater relative to precipitation and melt (Table 2) likely occurs through ET. Because this process occurs in the absence of geochemical reactions, we used Cl^- as a tracer to evaluate the hydrological processes controlling the spatiotemporal variability of hydrochemistry in the watershed.

4.2.2.2 *Reactive Sodium, Calcium, and Magnesium Processes*

In addition to atmospheric deposition and ET, concentrations of reactive ions, including Na^+, Ca^{2+}, and Mg^{2+}, are also influenced by mineral dissolution from soil and rock containing feldspar and pyroxenes minerals. Albite ($NaAlSi_3O_8$) and diopside ($CaMgSi_2O_6$) were chosen as representative model minerals from these groups, respectively, because they were prevalent across multiple samples, and the choice of two minerals enabled us to most simply produce observed concentrations throughout the watershed (Table 1). Other minerals containing elements with very low observed solute concentrations (e.g., Iron (Fe) and Manganese (Mn)) were not considered in order to focus on major elements. We represent kinetic dissolution of albite and diopside using parameters from literature with further manual adjustments to reproduce observed streamwater and groundwater solute concentrations and stream discharge (Table 3).

Mineral Dissolution	$log_{10}K_{eq}^{a}$	$log_{10}k^{b}$	SSA(m^s/g)^c
$NaAlSi_3O_{8(s)}$ (Albite) + $4H_2O$ + $4H^+$ $\rightarrow$ Na^+ + Al^{3+} + $3H_4SiO_4$	2.76	-10.9 (-9.89 – -11.9)	0.075 (0.02 – 1.09)
$CaMgSi_2O_{6(s)}$ (Diopside) + $2H_2O$ + $4H^+$ $\rightarrow$ Ca^{2+} + Mg^{2+} + $2H_4SiO_4$	20.96	-13.2 (-9.95 – -14.24)	0.086 (0.001 – 2.3)

[a] K_{eq} from the database EQ3/6 (Wolery, 1992)
[b] Calibrated dissolution rate constants, which fall within the range of values presented in Brantley et al. (2008) (shown in parentheses).
[c] Calibrated soil mineral specific surface area (SSA) values; these fall within the range of values presented in Brantley et al. (2008) (shown in parentheses).

Table 3: Dissolution reactions and kinetic and thermodynamic parameters for minerals included in the model. For comparison, values in parentheses are the range found in (Brantley et al., 2008).

4.3 Model Scenarios

The model was implemented for three different scenarios. In the first scenario, Na^+, Ca^{2+}, and Mg^{2+} were simulated as non-reactive ions along with Cl^-, in order to isolate the control of hydrological processes. In the second scenario, mineral dissolution was included to assess the impact of geochemical processes on the concentrations of Na^+, Ca^{2+}, and Mg^{2+}. To evaluate the role of glacier melt in controlling current hydrochemical conditions, we also tested a third scenario that includes geochemical processes without glacial meltwater. In the scenarios with mineral dissolution (2 and 3), we chose Na^+ as the representative diagnostic solute among the three dominant ions observed in the watershed (Na^+, Ca^{2+}, Mg^{2+}); simulation results of other ions were qualitatively similar to Na^+ results.

4.4 Model Calibration

Continuous hourly measured stream discharge from June 2015-June 2016 and the discrete measurements of Na^+, Ca^{2+}, Mg^{2+}, and pH on June 15, 2015, June 15, 2016, and February 20, 2017 were used for the model calibration. Na^+ is involved in albite dissolution, and Ca^{2+} and Mg^{2+} participates in diopside dissolution. To reproduce the stream discharge and major ion concentrations in groundwater and stream water, soil hydraulic properties (for the vegetated, non-vegetated, and ice-covered portions of the watershed), and mineral specific surface area were manually tuned. Monte

Carlo simulations with perturbations added to the final calibrated soil hydraulic parameters (shown in Table 4) were carried out to evaluate the sensitivity of the model performance to a range of plausible soil parameters and to provide a rough representation of uncertainty associated with the final simulations (details in the Supplementary Information, Section S-1).

	KINFV (m/s)	KSATV (m/s)	KSATH (m/s)	Porosity	Residual Moisture	α (1/m)	β (-)
Ice-covered	1.64E-7	4.56E-8	4.56E-7	0.296	0.05	0.412	1.038
Sparsely Vegetated	1.74E-7	4.85E-8	4.85E-7	0.296	0.05	0.437	1.038
Grassland	1.87E-7	5.27E-8	5.27E-7	0.297	0.05	0.469	1.039

Table 4: Parameters calibrated to match observed discharge and major ion concentrations in stream water and groundwater. Parameters include hydraulic conductivities for vertical infiltration (KINFV), vertical saturated flow (KSATV), horizontal saturated flow (KSATH), porosity, residual soil moisture, and shape parameters (α and β) for the van Genuchten moisture retention curve: $\theta = \theta_{res} + porosity \times \left(\frac{1}{1+|\alpha\psi|^{\beta}}\right)^{(1-\frac{1}{\beta})}$, with water content θ and pressure head ψ. The comparison of new versus previous soil hydraulic estimations from Saberi et al. (2019) are shown in the Supplementary Information, Table S2.

We relied on the widely used Nash-Sutcliffe efficiency (NSE) approach (Nash & Sutcliffe, 1970) to quantify model performance. Model results are considered satisfactory if 0<NSE<1, with NSE=1 as an indicator of a perfect match between observations and simulations (Moriasi et al., 2007). The traditional NSE is used here, which is calculated as follows (Nash & Sutcliffe, 1970):

$$NSE = 1 - \frac{\sum_{i=1}^{n} e_i^2}{(O_i - O_m)^2} \tag{4}$$

where, e_i is the error (Observed$_i$-Simulated$_i$) for location and time i, n is the number of measurements, O_i is the measurement at location and time i, and O_{mean} is the mean of all measurements.

4.5 C-Q Power Law Model

The concentrations (C) of non-reactive and weathering-derived solutes exported from a watershed may depend on stream discharge (Q) (Shanley et al., 2011; R. F. Stallard & Murphy, 2014) or remain relatively time-invariant (chemostatic) depending on the processes within the watershed controlling them (Hem, 1985; Johnson et al., 1969; Godsey et al., 2014; Li et al., 2017). The relationship between solute concentrations and stream discharge is often fit to a power law relationship (Godsey et al., 2009):

$$C = aQ^b \tag{5}$$

where a and b are fitted parameters. b has been found to vary from -1 to +0.4 (Godsey et al., 2009; Herndon et al., 2015). The C-Q relationships are often considered chemostatic when b ranges between -0.2 and +0.2, while pure dilution (non-chemostatic end-member) occurs when b is equal to -1.

To investigate the influence of glacial melt on the hydrochemistry of the watershed, we compare C-Q power law model fit to simulation results with meltwater and without meltwater. Although C-Q analysis is typically applied to continuous measurements, here we rely on model simulations to overcome data sparsity and to explore different scenarios.

5 Results and Discussion

5.1 Calibration Results

Calibration results for geochemical reaction parameters and soil hydraulic parameters are shown in Tables 3 and 4, respectively. Simulated stream discharge matches observed discharge with an NSE coefficient of 0.87, which indicates that the model performance is satisfactory (Figure 3a). Constraining the model simulations on observed hydrochemical concentrations in addition to stream discharge resulted in lower calibrated porosity and van Genuchten parameters than those used in Saberi et al. (2019) (Table S2). As noted above, in Saberi et al. (2019), only discharge data were directly used in the parameter calibration, while hydrochemical data were indirectly considered through model constraints on estimates of melt and groundwater contributions from a mixing model. The newly calibrated hydraulic parameters in this study resulted in lower groundwater retention and correspondingly higher groundwater contribution to streamflow.

The calibrated model results further show that lateral groundwater flow, which contains both precipitation and glacial meltwater, contributes on average 78% of streamflow (Figure 3a), with surface runoff contributing the remaining 22%. In comparison, Saberi et al. (2019) determined a 45% groundwater contribution to streamflow using Flux-PIHM, which was calibrated to be consistent with mixing model estimates of melt and groundwater contributions (Figure 4a). The hydrochemically constrained RT-Flux-PIHM model in this study and the mixing model in Saberi et al. (2019) use the same hydrochemical observations from the Gavilan Machay watershed, but the difference in the groundwater contribution estimates arises because the mixing model relied on few samples from readily accessible springs in lower reaches of the watershed to represent the groundwater end-member throughout the entire watershed. In contrast, the distributed RT-Flux-PIHM model appropriately accounts for spatially variable groundwater concentrations, which differ substantially with elevation as groundwater moves from headwater areas toward the discharge point, due to increasing contact time with reactive minerals. Comparison of these results demonstrates the importance of hydrochemical model constraints in addition to hydrological constraints. In the RT-Flux-PIHM results, stream discharge closely follows the temporal trends of groundwater discharge to the stream (coefficient of correlation of 0.79), indicating that simulated stream flow is predominantly controlled by groundwater (Figure 3a). The lateral groundwater flow to the stream is further positively correlated with the precipitation plus melt over time (coefficient of correlation of 0.65), which suggests that precipitation and ice melt that infiltrate travel relatively fast to the stream such that their temporal variability is not significantly dampened and lost in the subsurface (Figure 3b).

Direct model calibration to hydrochemical data not only improved the constraint on groundwater contributions to the stream, but also on melt-groundwater interactions. The estimate of discharge originating from meltwater that first infiltrates and travels as groundwater before flowing to streams increased from 16% to 37% after constraining the model on hydrochemical observations (Figure 3c and 4b). Following Saberi et al. (2019), the percent melt contribution to the groundwater is calculated using simulation scenarios with and without ice melt:

$$\%MeltInGroundwater = \frac{Groundwater_{WithIceMelt} - Groundwater_{WithoutIceMelt})}{Groundwater_{WithIceMelt}} \tag{6}$$

where $Groundwater_{WithIceMelt}$ and $Groundwater_{WithoutIceMelt}$ is the lateral groundwater contribution to the stream in scenarios with and without ice melt, respectively. New hydrochemically constrained simulations show that as the temperature increases during the El Niño event, the ice melt contribution to the groundwater increases (Figure 3d).

Overall, this result demonstrates that incorporating hydrochemical data in the model calibration constrains flow pathways and impacts partitioning of both stream discharge and meltwater. Constraining the model simulations on hydrochemical data results in higher meltwater contribution to groundwater and higher groundwater contribution to the streamflow (Figure 4).

To evaluate the role of geochemical reactions in simulating observed hydrochemical conditions, we compared Na^{+}, Ca^{2+}, and Mg^{2+} concentrations in groundwater in scenarios with and without mineral dissolution. The results show that without mineral dissolution, meteoric and melt inputs and ET could account for only 14-16% of the time-average concentrations, and that mineral dissolution was needed in the model to match observed groundwater concentration ranges at different locations within the watershed (Figure 5).

Figure 6 shows the calibrated concentrations of all three major ions at the outlet, which match reasonably well with measured concentrations during the 2015 and 2016 field campaigns. The cali-

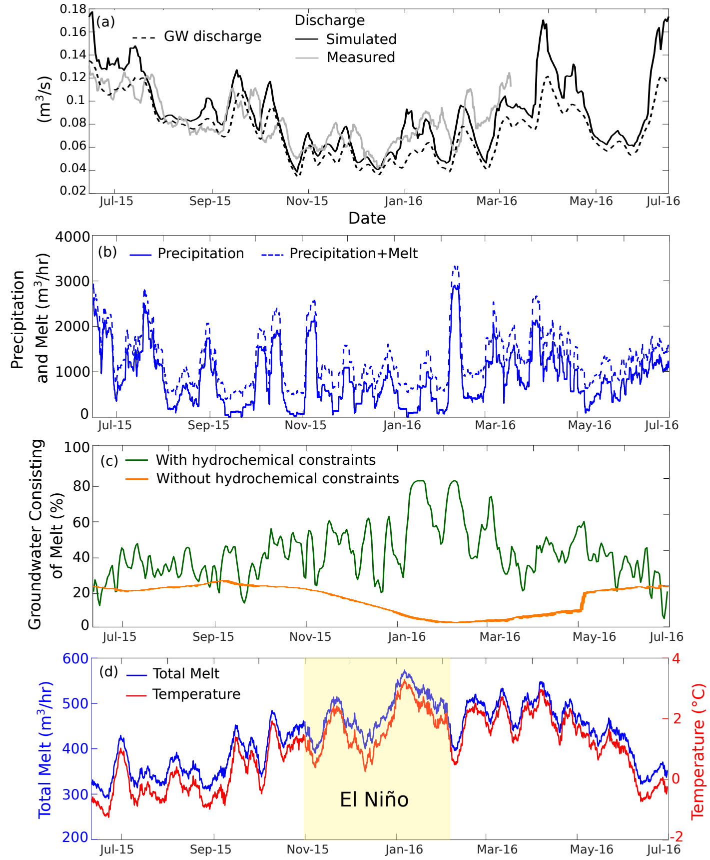

Figure 3: Temporal variability of a) simulated stream discharge, measured stream discharge, and groundwater discharge to the stream, b) precipitation (solid line) and precipitation + ice melt (dashed line), c) percentage of groundwater that constitute ice melt, d) average air temperature over the ablation zone (glacier-covered areas below the ELA (5050 m a.s.l.)) and simulated glacier melt production. The blue box demonstrated the time period during which an El Niño event occured over the watershed. The x-labels indicate the start of the corresponding month.

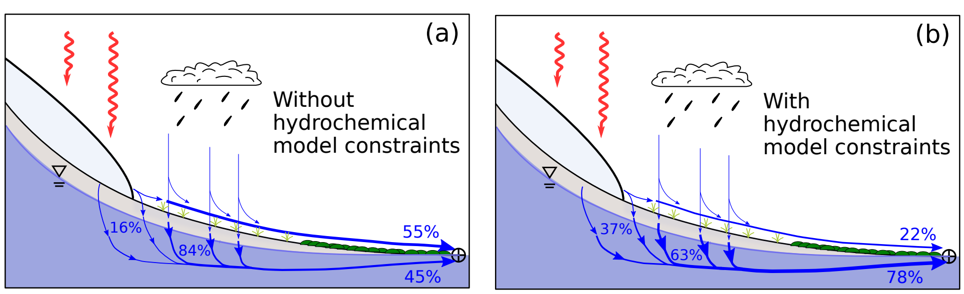

Figure 4: Groundwater partitioning between glacier melt and precipitation inputs, and stream discharge partitioning between surface runoff and groundwater. Model results for two cases are shown: a) without directly constraining the model on hydrochemical data versus b) with direct constraints on hydrochemical data.

bration results for the Na^+ concentrations along the stream sampling points SW-1, SW-2, and SW-3 (locations shown in Figure 2a) are presented in the Supplementary Information (Figure S2).

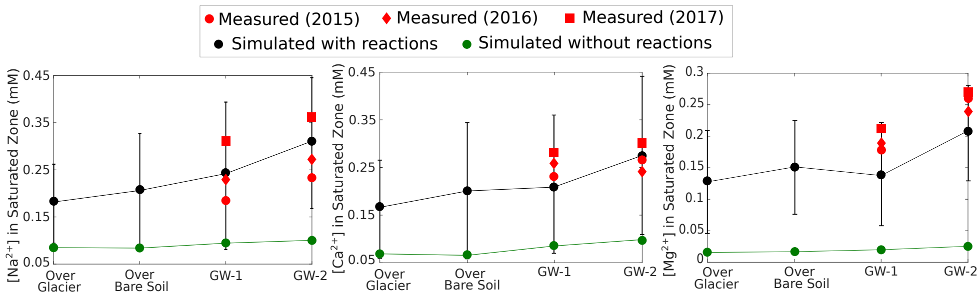

Figure 5: Simulated groundwater concentrations of Na^{+}, Ca^{2+}, and Mg^{2+} along an elevation gradient for two different scenarios, with and without geochemical reactions, along with measured ion concentrations. Ion concentrations were measured at the GW-1 and GW-2 spring locations (locations shown in Figure 2a). Simulated concentrations averaged over glacierized (ranges from 5300-6280 m.a.s.l) and bare soil cells (ranges from 4600-4900 m.a.s.l) were chosen to demonstrate the changes in concentrations simulated in the upper and middle parts of the watershed, where we lack groundwater samples. The error bars around the calibrated simulation results with reactions show a plus or minus one standard deviation interval from the Monte Carlo uncertainty simulations.

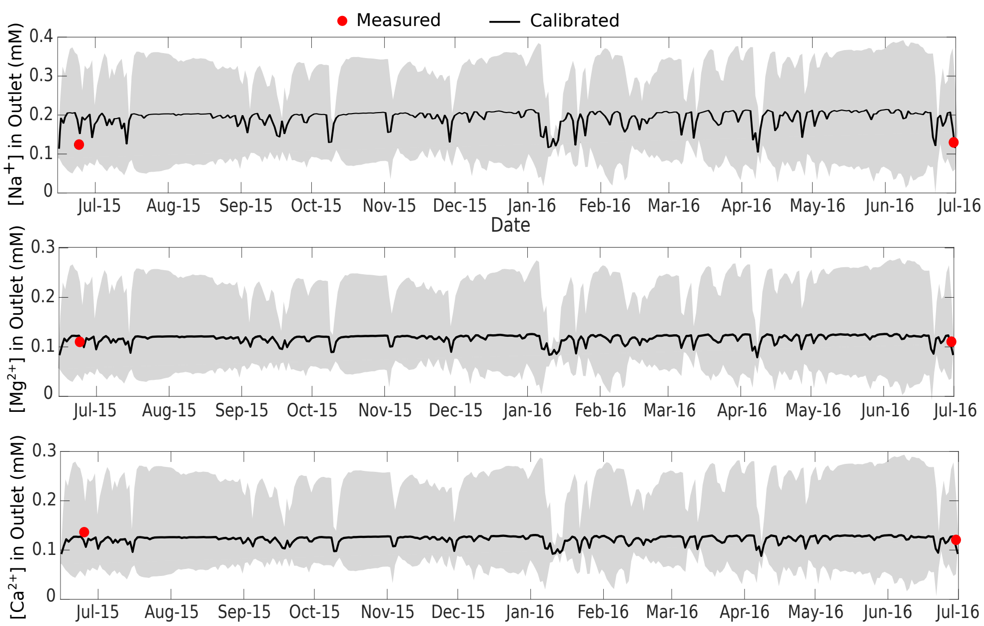

Figure 6: Simulated Na^{+}, Ca^{2+}, and Mg^{2+} in the outlet (calibrated result in black lines) compared to the measured concentrations at the SW-4 site (Figure 2a). Gray shaded areas show a plus or minus one standard deviation interval from the Monte Carlo uncertainty simulations.

5.2 Hydrological Controls on Subsurface Chemistry

To isolate the impact of hydrological processes on the hydrochemistry of the watershed, we examined Cl^{-} transport and its groundwater concentration variations arising from different hydrologic fluxes, including infiltration (diluting effect) and ET (concentrating effect). A simple mass balance assuming steady-state helps demonstrate the relative controls of the hydrologic fluxes on groundwater concentrations:

$$C_p \times Infiltration = C_g \times (I - ET) \tag{7a}$$

$$I = (Precipitation + Melt) - Runoff - SurfaceEvaporation \tag{7b}$$

where C_p is the Cl^- concentration in precipitation, C_g is the average Cl^- concentration in the saturated and unsaturated zones, I is infiltration, and ET is evapotranspiration. Eq. 7a can be rearranged to show the dependence of groundwater concentrations of Cl^- on the ratio of ET to infiltration (higher ratio results in higher groundwater concentration):

$$C_g = \frac{C_p}{(1 - \frac{ET}{I})} \tag{7c}$$

The model shows that the highest ET occurs within the vegetated parts of the watershed (Figure 2 and Figure 7a), with a maximum annual average of 2.4 mm/day. High ET and relatively lower infiltration rates in the vegetated area (Figure 7b) results in high ET to infiltration ratios (Figure 7c), which lead to increased Cl^- concentrations in groundwater (maximum of 0.065 mM) in these regions (Figure 7d).
Within the ice-covered area, not only is ET lower than in vegetated regions (Figure 7a), but infiltration rate is also higher (Figure 7b) due to high glacial melt rates, which are greater than the precipitation rate in most of the watershed. This results in very low ET to infiltration ratios (Figure 7c), thus generating some of the lowest concentrations in the watershed (Figure 7d).

5.3 Geochemical Controls on Hydrochemistry

5.3.1 Temporal Patterns

The sources of Na^+ in the model simulations include Na^+ production by mineral dissolution (R_p) and Na^+ input from glacial melt and rainfall (R_{mr}). R_p is the Na^+ production rate through albite dissolution, which was calculated by:

$$R_p = \frac{C_{Albite_t} - C_{Albite_{t-1}}}{dt} \tag{8}$$

where the increment in time is 1 day and C_{Albite} is the concentration of albite at time t. The Na^+ input from glacial melt and rainfall (R_{mr}) is the product of the melt plus precipitation rate, the Na^+ concentration in the precipitation, and the grid cell area. Watershed-scale values for R_p and R_{mr} were determined by summing over all grid cells. The Na^+ export rate (R_e) is the product of stream discharge and Na^+ concentrations at the stream outlet. As can be seen in Figures 8a and b, the simulated R_e primarily follows the stream discharge pattern (correlation coefficient of 0.88), which suggests that the discharge is the stronger driver of export rate variability over time than the concentration of Na^+ at the outlet. This is because Na^+ concentration at the outlet is relatively constant year-round (coefficient-of-variation of 13%) compared to the variability in discharge (coefficient-of-variation of 44%) (Figure 7c).

The low simulated variability of Na^+ concentrations at the outlet is largely due to groundwater-related processes. The importance of the subsurface is evident when comparing the different Na^+ input and output magnitudes. In the model, the production of Na^+ via mineral dissolution (average 1.68x109 mg/d) is much higher than meteoric and glacier melt inputs of Na^+ (average 1.8x107 mg/d), contributing to the vast majority of Na^+ export at the outlet (average 3.6x108) (note that excess Na^+ inputs are added to groundwater storage of Na^+ over the simulation period). However, during the dry period (November-February), even though lower groundwater storage (Figure 3b) leads to a decline in Na^+ production (Figure 8b), high ET concentrates Na^+ in groundwater (Figure 8a and c). During the wet periods (June-October and March-May), higher groundwater storage (Figure 3b) results in higher wetted surface area of minerals, thereby supporting higher albite dissolution rates and Na^+ production, which somewhat compensates for dilution by high precipitation and melt events (Figure 8b). However, overall, ET has a prevailing effect on concentrations during the wet period as well. Na^+ production by albite dissolution to some degree modulates concentrations during the wet period,

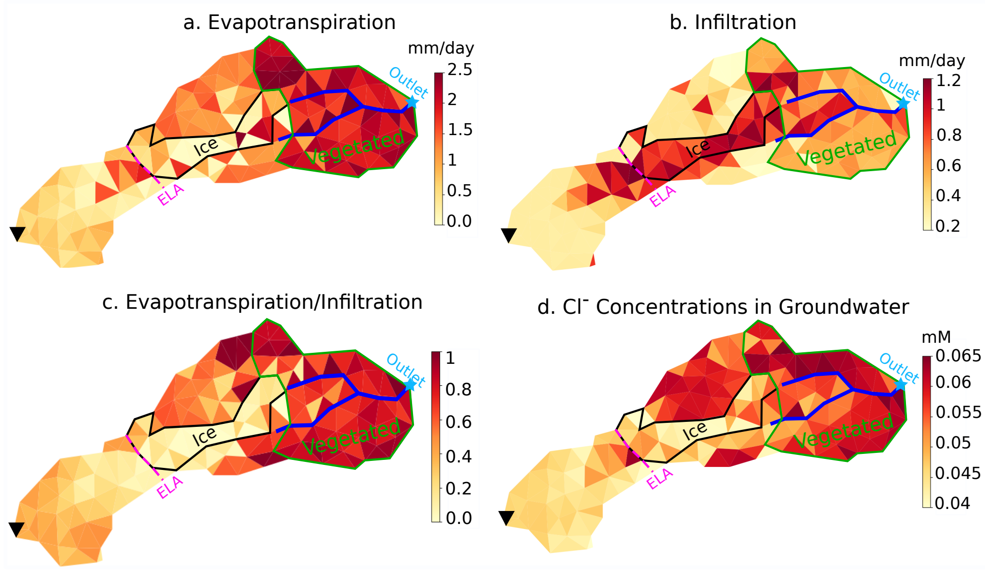

Figure 7: Time-averaged model results over each grid cell. a) ET, b) infiltration (as defined in text), c) ratio of ET to infiltration, and d) Cl^- concentrations averaged over saturated and unsaturated zones. The black triangle shows the peak of Volcán Chimborazo (6280 m a.s.l.). The dashed pink line represents the ELA at 5050 m a.s.l. The black outline indicates the glacierized grid cells below the ELA, in which glacier melt is applied in model. The green outline identifies the vegetated part of the watershed. The blue line shows the stream channel, and the blue star indicates the outlet.

but the concentrations in groundwater are still lower than those during the dry period due to lower ET during the wet period (Figure 8c).

Higher simulated variability in stream chemistry (coefficient-of-variation of 13%) compared to groundwater chemistry (coefficient-of-variation of 2%) suggests that surface water dilution via runoff contribution to the stream may still have an impact (Figure 8c). However, the temporal variation of stream chemistry is primarily controlled by the percentage groundwater contribution to the stream (correlation coefficient of 0.79) (Figure 8c). As noted above (Section 5.1), lateral groundwater is positively correlated with precipitation plus melt inputs, which together indicates that large precipitation and melt events promote solute export via flushing of solutes stored in groundwater.

5.3.2 Spatial Patterns

Figure 9 shows the spatial distribution of simulated hydrological and geochemical variables, averaged over separate wet and dry seasons, to probe different processes controlling the spatial variability of the hydrochemistry over different hydrological conditions. Throughout the year, ET is highest over the vegetated parts of the watershed due to plant transpiration, and soil moisture is highest in the convergent areas and adjacent to the stream (Figure 9). The spatial pattern of Na^+ concentrations in groundwater follows both ET and Na^+ production rates in the model, which suggests that these two fluxes have a combined impact on the spatial variability of Na+ in groundwater. Multivariate regression analysis showed that on average (throughout the year and over the entire watershed), 69% of the spatial variability in groundwater concentrations can be explained by ET and 31% by production via albite dissolution, with precipitation and melt inputs having negligible impact.

Interestingly, while correlation results show that Na^+ production via albite dissolution plays a secondary role in explaining the spatial variability of Na^+ concentrations in groundwater relative to ET, production is in fact the predominant controller of the spatial mean concentration in the model. Specifically, the mean groundwater Na^+ concentration over the watershed increases nearly six-fold with albite dissolution in the model, from 0.03 mM to 0.17 mM. This result is not surprising consid-

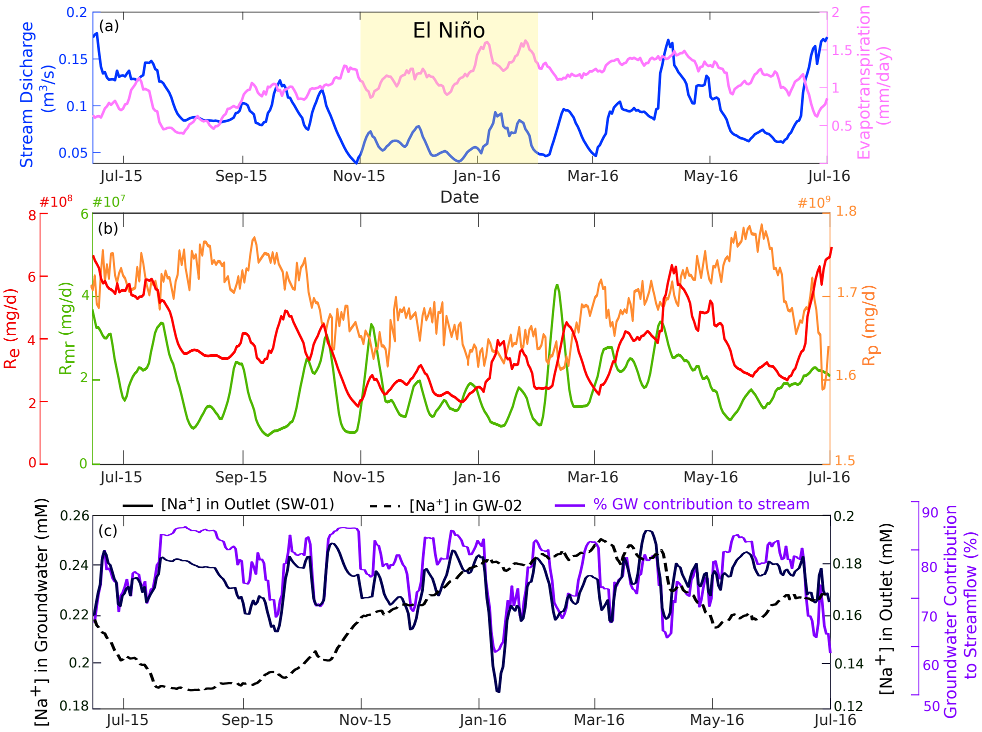

Figure 8: Temporal variability of a) stream discharge and ET, with the warm and low-precipitation El Niño period shaded yellow; b) Na^+ input by precipitation and melt events (R_{mr}), Na^+ export rate at the outlet (R_e), and Na^+ production rate by albite dissolution (R_p); and c) Na^+ concentration in groundwater (at sample site GW-2 shown in Figure 2a), Na^+ concentration in the outlet (sampling site SW-4 shown in Figure 2a), and percentage of groundwater contribution to streamflow. The blue box demonstrated the time period during which an El Niño event occured over the watershed.

ering total watershed results in Figure 8 show that production comprises the vast majority of all mass inputs of Na^+ into the watershed. Further, when compared to ET, dissolution appears to account for more of the overall concentration gradient with topography around the stream channel. Calibrated simulations with mineral dissolution show a groundwater concentration gradient of 0.045 mM/km a.s.l. for Na^+ from below the glacierized headwaters at 5200 m a.s.l. to below the lower stream reach at 4100 m a.s.l. (GW-2) (Figure 3). In comparison, the model scenario without mineral dissolution resulted in less than half the concentration gradient (0.018 mM/km a.s.l.) over the same interval, demonstrating that alone, ET effects explain a smaller portion of the concentration changes over the full watershed extent of the stream channel. Together, the spatial analysis shows that production via mineral dissolution plays the major role in explaining spatial mean concentrations of reactive solutes and concentration gradients along the full extent of the stream channel, while ET is the better predictor of finer scale spatial variability among all grid cells.

To examine the processes behind the relative contributions of ET and mineral dissolution to solute concentrations across the watershed, we looked at potential interactions between ET and dissolution. For example, the apparent control of ET on the finer scale spatial variability of Na^+ groundwater concentrations could in fact be driven by production, because higher ET can lead to lower flow and longer contact times that facilitate mineral dissolution. However, a weak spatial correlation between ET and Na^+ production (correlation coefficient of 0.15) suggests that this is not a major phenomenon in the model simulations. Instead, Na^+ production strongly follows soil moisture content (correlation coefficient of 0.89 over space), which does lead to higher groundwater concentrations along the

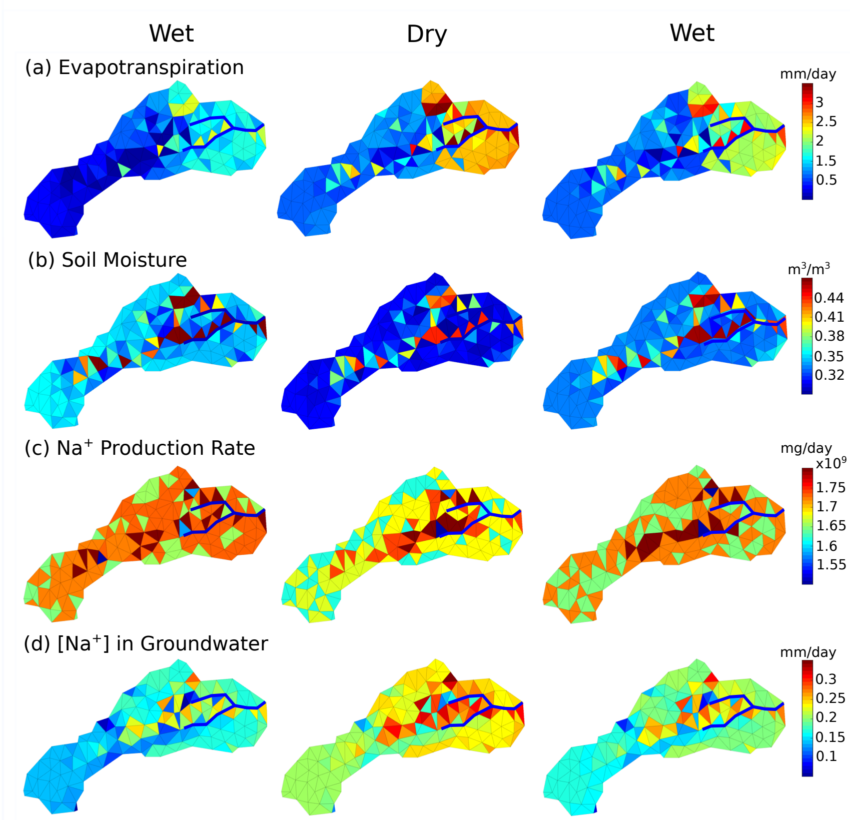

Figure 9: a) ET, b) Soil Moisture, c) Na^+ production rate, and d) Na^+ concentration in groundwater averaged over three time periods (June-October, November-February, March-May).

stream and in convergent areas where soil moisture content is close to the saturation (Figure S3). However, it appears that overall spatial variability of concentrations among all grid cells is mostly controlled by ET via direct removal of soil moisture. Further evaluation reveals that some of the apparent dissolution controls on large-scale Na^+ groundwater concentrations (spatial mean and gradient over the extent of the watershed) in fact involve ET processes. This can be understood with the following steady-state mass balance equation for reactive solutes, which is a straightforward extension of the non-reactive case for Cl^- (equations 7aa and 7c):

$$C_g = \frac{R_p + C_p \times I}{I - ET} \tag{9a}$$

$$C_g = \frac{\frac{R_p}{I}}{1 - \frac{ET}{I}} + \frac{C_p}{1 - \frac{ET}{I}} \tag{9b}$$

where C_g is the Na^+ concentration in groundwater, R_p is the Na^+ production rate through albite dissolution, C_p is the Na^+ concentration in precipitation and meltwater, I is the infiltration, and ET is evapotranspiration. From the first term on the right hand side of equation 9b, it can be seen that with ET>0, the Na^+ input from dissolution (R_p) is amplified by a factor of $\frac{1}{1-\frac{ET}{I}}$ when determining the groundwater concentration. This multiplicative amplification effect likely explains why ET plays such an important role in controlling the fine scale spatial variability throughout the watershed, even though dissolution serves as the major source of solute mass over the watershed. This interaction underscores the importance of representing both geochemical and hydrological processes when

considering hydrochemical controls in a watershed. Our results also show that in heterogeneously vegetated watersheds, such as those in high mountain environments with a discrete vegetation line, ET variability can play a much larger role in controlling hydrochemical variability compared to sites with relatively homogeneous land cover and ET (e.g., Li et al. (2017); Zhi et al. (2019).
Broadly throughout the watershed, high soil moisture results in high Na+ production rates during the wet seasons, with opposite results in the dry El Niño period (Figure 9a, b, and c). However, as noted with the time series results for watershed-scale fluxes in Figure 8, Na^+ concentrations in groundwater were on average highest during this dry period due to high ET and low contribution of dilute precipitation and ice melt to the watershed (Figure 9a and d). Spatial results further demonstrate that over the dry period, the heterogeneity of the soil moisture content and production increases over the watershed, with convergent areas and stream valleys having much higher productivity relative to the rest of the watershed.

5.4 Control of Glacier Meltwater on Na^+ Production and Export

5.4.1 C-Q Power Law Model

For simulations with meltwater, the relationship between stream discharge and the simulated Na+ concentrations at the outlet is considered to be chemostatic based on a C-Q slope of -0.08 on a log-log scale (Fig 10a). However, in Gavilan Machay, various dilution events also occur, and nearly all of these (especially those with lowest concentrations) correspond to times of high surface runoff contribution to discharge (Figure 10b). In particular, peak runoff contributions drive these dilution events, which can occur any time of the year (Figure 10c). In simulations without glacier melt, peak discharge and surface runoff contributions to discharge decrease. Overall Na^+ concentrations in groundwater increase, and almost all of the strongest dilution events disappear (Figure 10d, e, and f), making the C-Q relationship even more chemostatic (slope of -0.011 on a log-log scale) (Figure 10d). Torres et al. (2015) also found the C-Q relationship in non-glacierized, steep Andean catchments to be chemostatic, potentially due to higher erosion rates and correspondingly higher dissolution rates during peak flow. Comparison of the two model scenarios suggests that glacier melt produces some of the largest surface runoff events in Gavilan Machay. These events can produce diluting episodes in an otherwise chemostatic environment in which precipitation events mobilize solutes from highly reactive subsurface minerals. It can also be seen that the melt-driven dilution events can occur anytime because of year-round ablation in the tropics (Figure 3d). This is distinct from temperate systems where glacier melt does impose a strong seasonal control on the hydrochemistry of the watershed (e.g. Lewis et al. (2012); Stachnik et al. (2016)).
These model results indicate that the C-Q patterns are driven by the relative control of two end-member sources of water. Streamflow is primarily derived from two sources with distinct chemistry: surface runoff with low Na^+ concentrations and groundwater lateral flow with higher Na^+ concentrations. In the with-ice meltwater scenario, melt inputs lead to times when the ratio of surface runoff to groundwater contribution to the stream is very high, and this produces a diluting effect. A similar behavior was observed in simulations at the Coal Creek study watershed, where the C-Q relationship was found to depend on the switching dominance among three end-members (surface runoff, shallow groundwater, and deep groundwater) and the distinction among their chemistries (Zhi et al., 2019). Without ice melt, Gavilan Machay is governed by a single end-member, lateral groundwater flow, which results in much more chemostatic conditions; this is similar to RT-Flux-PIHM findings by Li et al. (2017) for the Shale Hills study watershed. Higher groundwater contributions to streamflow generate steadier and higher stream concentrations, because of less dilution by surface runoff. These findings suggest that after glaciers fully retreat, the concentrations of major ions and nutrients in the stream may increase and stabilize, though exact changes will also depend on future precipitation and temperature.

5.5 Glacial Meltwater Influence on Hydrogeochemical Processes

To further probe processes controlling the C-Q relationships as well as their downgradient implications, we examine catchment-scale production and export rates, and Na^+ concentrations in ground-

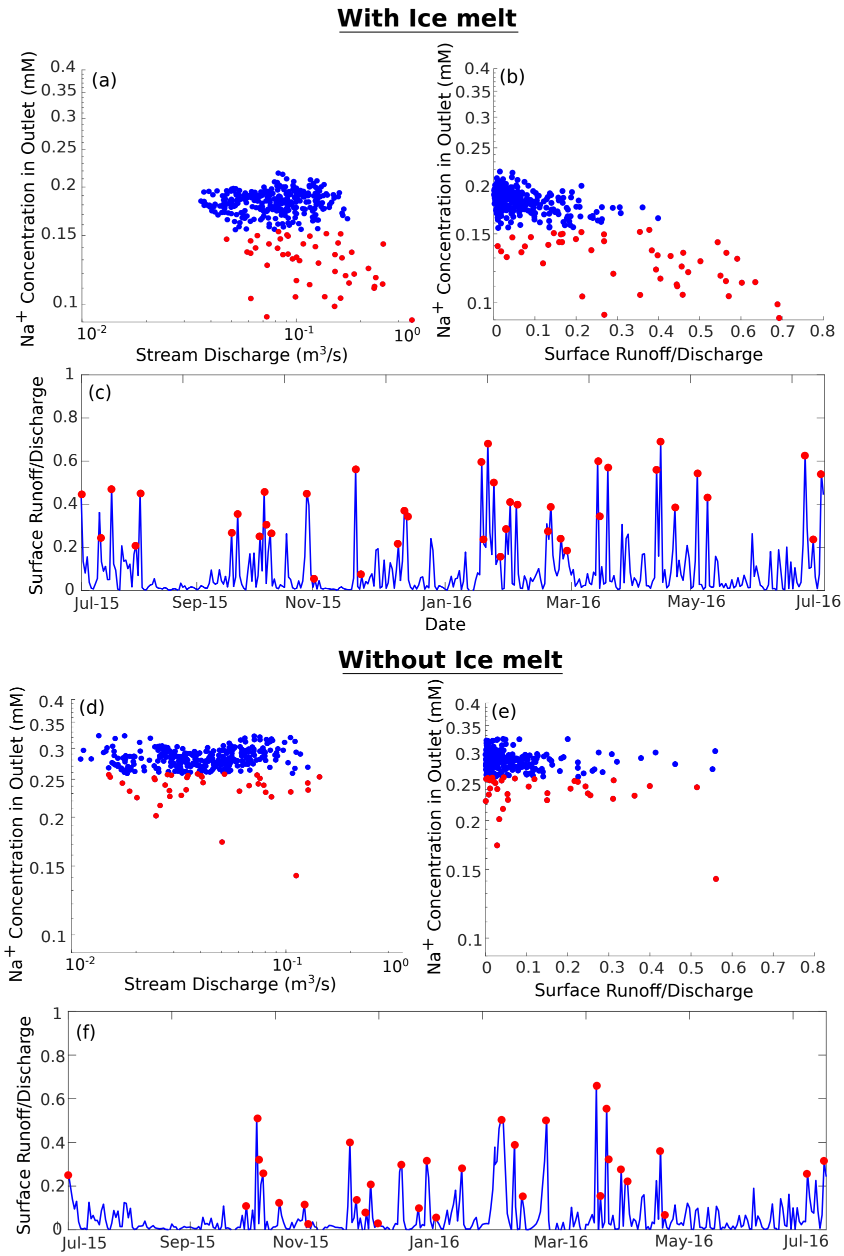

Figure 10: The relationship between simulated streamflow and simulated Na+ concentrations at the outlet, with ice melt (a) and without ice melt (d). The relationship between the contribution of surface runoff to stream discharge (fraction of total discharge) and simulated Na^{+} concentrations at the outlet, with ice melt (b) and without ice melt (e). The contribution of surface runoff to discharge (fraction of discharge) over time, with melt (c) and without ice melt (f). Red dots are the points at which the Na^{+} concentrations in outlet are less than one standard deviation below the mean value due to high runoff contribution to streamflow.

water and at the outlet in the scenarios with and without glacier melt (Figure 10). For Na^{+}, excluding ice melt leads to a decrease in Na^{+} input with wet deposition (defined as the combined input from ice melt and precipitation) (Figure 11a), lower groundwater storage, lower soil water content, and lower Na^+ production rate through albite dissolution (Figure 11b). However, even though wet deposition and production decrease, Na^+ concentrations in groundwater increases by 55% in the scenario without glacial melt (Figure 11d), due to the 170% higher ET to infiltration ratio (Figure 11c). The groundwater contribution to streamflow increases from 80% of the total discharge to 95% in the no melt scenario, although the absolute value of groundwater flow into the stream decreases by 41% without meltwater infiltration (Figure 11e). The increase in groundwater concentrations leads to 51% higher Na^+ concentrations in the stream (Figure 11f), due to the dominance of groundwater contributions to total streamflow in no-melt scenario.

Even though Na^+ concentrations in streamflow are higher without meltwater, this cannot offset the

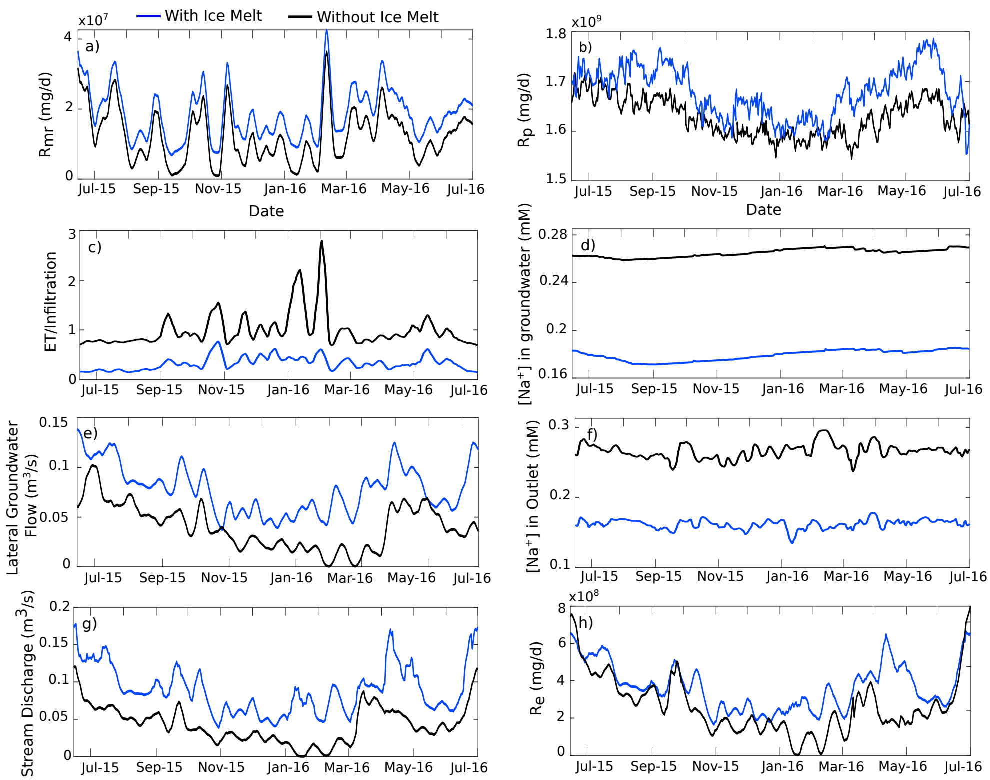

Figure 11: a) Na^+ input via melt and precipitation, b) Na^+ production rate via albite dissolution, c) the ratio of ET over infiltration, d) Na^+ concentrations in groundwater, e) groundwater discharge to the stream, f) Na^+ concentrations in the outlet, g) stream discharge, and h) Na^+ export rate (C*Q). The blue line represents the scenario with melt and black like the scenario without glacial melt.

decrease in discharge when determining changes in export rates. Without glacier melt, time-average stream discharge decreases by 45% compared to the scenario with melt (Fig 11g). This results in 23% lower export of Na^+ in the no-melt scenario (Figure 11h). This corresponds with findings based on a global data compilation that weathering yields are generally greater in glacierized watersheds compared to non-glacierized due to higher discharge, while solute concentrations are lower (Torres et al., 2017). Consistent with temporal variability findings in Section 5.3.1, the solute export rate conditions under melt versus no-melt scenarios appear to be controlled primarily by stream discharge and secondarily by groundwater contributions to streamflow.

6 Summary and Conclusion

Our work highlights the complex hydrochemical responses of a tropical glacierized mountainous watershed on Volcán Chimborazo at different temporal and spatial scales controlled by hydrological and geochemical processes. Results indicate that model calibration to hydrochemical data in addition to hydrological data provides a better constraint on subsurface flow pathways. Our newly calibrated simulations show that total lateral groundwater flow contributed 78% of stream discharge, and that 37% of the total glacier melt directly contributes to groundwater flow.

Due to the presence of highly reactive silicate minerals, geochemistry plays an important role in controlling the hydrochemistry of the watershed. Mineral dissolution comprises most of the mass input of reactive ions such as Na^+ into the watershed, while wet deposition via precipitation and melt provides orders of magnitude less. As the major source, mineral dissolution controls the spatiotemporal mean groundwater concentration of reactive ions in the watershed, and it accounts for much of the gradient in groundwater concentrations with topography over the extent of the stream network.

Because mineral dissolution most directly influences groundwater chemistry, hydrological processes in the subsurface and groundwater-surface water interactions also play an important role in controlling the hydrochemistry of the watershed, including stream chemistry. Over the course of the year, dissolution rates are highest during the wet seasons, when high soil moisture allows for higher wetted surface area of minerals. But groundwater concentrations of reactive ions are relatively constant throughout the year (coefficient-of-variation of 2%) due to the offset effect of ET; ET is highest in the dry season, boosting concentrations even when production through mineral dissolution is low. Because groundwater flow to streams comprises a large fraction of total discharge, stream water concentrations of reactive ions are strongly controlled by groundwater contributions to the stream (temporal correlation coefficient of 0.79). Groundwater flow is fast, such that infiltration of large precipitation and melt events flush high solute concentrations from the subsurface into the stream. This flushing leads to higher temporal variability in stream water concentrations than groundwater concentrations (13% versus 2% coefficient-of-variation). This is still a much lower variability than in stream discharge (44% coefficient-of-variation). As a result, temporal variability in the export (concentration times discharge) of reactive ions is driven primarily by variations in discharge rather than concentration.

Although dissolution controls bulk amounts of reactive solutes in the watershed, ET plays the major role in determining the spatial variability in groundwater concentrations across the watershed. This spatial control by ET is especially pronounced because of the sharp gradient in vegetation, and similar effects may be expected in other steep, high-elevation watersheds with discrete vegetation lines. The spatial control by ET is likely heightened by interactions between ET and production via dissolution; the concentrating effect of ET includes a multiplicative amplification of the production rate based on the ratio of ET to infiltration. ET also serves as the dominant factor determining seasonal variability of groundwater concentrations; dry seasons have on average higher concentrations of reactive ions due to concentrating effects, despite lower production rates.

Because of year-round ablation in the tropics, glacier melt does not appear to be an important seasonal driver of hydrochemical variability. However, glacier melt does exert a unique influence on the C-Q relationship in the watershed. A model scenario test that omits glacier melt inputs exhibits strongly chemostatic behavior, consistent with past studies in non-glacierized, steep Andean watersheds in the tropics (Torres et al., 2015). In comparison, simulations with glacier melt have higher peak surface runoff, and times of high surface runoff contributions to streamflow produces strong dilution episodes superimposed on an otherwise chemostatic C-Q graph. These C-Q patterns reflect the relative control of two end-member sources of water contributing to the stream, dilute melt-driven surface runoff and higher-concentration groundwater. This result is similar to the multiple end-members noted by Zhi et al. (2019) that control the degree of chemostasis in simulations at the Coal Creek study watershed, based on the distinction of their chemistries. Without melt, the watershed reverts to a mostly single-member system dominated by groundwater, which produces much more constant concentrations over time.

Melt inputs also decrease concentrations of reactive ions in the stream due to overall dilution while increasing discharge throughout the year. The difference in discharge dominates the difference in concentration, leading to a higher export of reactive ions from the watershed with melt, consistent with a global study showing higher weathering yields in glacierized watersheds compared to non-glacierized (Torres et al., 2017). This suggests that with the retreat of glaciers, export of reactive ions, including nutrients, may decrease even if stream concentrations increase due to higher ET relative to infiltration, which may have implications for downstream ecosystems. Actual changes, however, will depend on other future changes in temperature, precipitation, and vegetative cover.

Acknowledgments

Funding from NSF (EAR-1759071) supported this work. Saberi also received financial support from University of Minnesota. The authors would like to acknowledge Daniel Stanton and Andy Wickert (University of Minnesota) for helpful discussions; Chloe Shaw and Emily Carlson (Gustavus Adolphus College) for fieldwork help; Carla Manciati, Xavier Zapata, and Veronica Minaya (Escuela Politecnica Nacional, Quito) for assistance in field site access; and Scott Alexander (University of Minnesota) for lab support. The Flux-PIHM version 0.10.0 used for this paper is available on GitHub, at https://github.com/PSUmodeling/MM-PIHM/releases/tag/v0.10.0-alpha. Field data collected and used in this work is available at: https://www.hydroshare.org/resource/d390906d0ed8440b9e3df8c48075c454/

References

Andermann, C., Longuevergne, L., Bonnet, S., Crave, A., Davy, P., & Gloaguen, R. (2012, 1). Impact of transient groundwater storage on the discharge of Himalayan rivers. *Nature Geoscience*, *5*(2), 127–132. doi: 10.1038/ngeo1356

Bao, C., Li, L., , Shi, y., & Duffy, C. (2017). Understanding watershed hydrogeochemistry: 1. development of rt-flux-pihm. *Water Resources Research*, *53*(3), 2328–2345.

Baraer, M., McKenzie, J., Mark, B. G., Gordon, R., Bury, J., Condom, T., … Fortner, S. K. (2015, 5). Contribution of groundwater to the outflow from ungauged glacierized catchments: a multi-site study in the tropical Cordillera Blanca, Peru. *Hydrological Processes*, *29*(11), 2561–2581. doi: 10.1002/hyp.10386

Baraer, M., McKenzie, J. M., Mark, B. G., Bury, J., & Knox, S. (2009, 10). Characterizing contributions of glacier melt and groundwater during the dry season in a poorly gauged catchment of the Cordillera Blanca (Peru). *Advances in Geosciences*, *22*, 41–49. doi: 10.5194/adgeo-22-41-2009

Barba, D., Robin, C., Samaniego, P., & Eissen, J.-P. (2008). Holocene recurrent explosive activity at chimborazo volcano (ecuador). *Journal of Volcanology and Geothermal Research*, *176*(1), 27–35.

Barba, D., Samaniego, P., Eissen, J.-p., Robin, C., Fornari, M., Cotten, J., & Beate, B. (2005). Geology and structure of the late Pleistocene to Holocene Chimborazo stratovolcano (Ecuador). *6th International Symposium on Andean Geodynamics (ISAG 2005, Barcelona)*(January), 90–93.

Barnett, T. P., Adam, J. C., & Lettenmaier, D. P. (2005, 11). Potential impacts of a warming climate on water availability in snow-dominated regions. *Nature*, *438*(7066), 303–309. doi: 10.1038/nature04141

Baronas, J. J., Torres, M. A., Clark, K. E., & West, A. J. (2017). Mixing as a driver of temporal variations in river hydrochemistry: 2. major and trace element concentration dynamics in the andes-amazon transition. *Water Resources Research*, *53*(4), 3120–3145.

Bartoli, F., Poulenard, A., & Schouller, B. (2007). Influence of allophane and organic matter contents on surface properties of andosols. *European journal of soil science*, *58*(2), 450–464.

Benettin, P., Bailey, S. W., Campbell, J. L., Green, M. B., Rinaldo, A., Likens, G. E., … Botter, G. (2015). Linking water age and solute dynamics in streamflow at the h ubbard b rook e xperimental f orest, nh, usa. *Water Resources Research*, *51*(11), 9256–9272.

Bhatt, G., Kumar, M., & Duffy, C. J. (2014, 12). A tightly coupled GIS and distributed hydrologic modeling framework. *Environmental Modelling & Software*, *62*, 70–84. doi: 10.1016/j.envsoft.2014.08.003

Bradley, R. S. (2006, 6). CLIMATE CHANGE: Threats to Water Supplies in the Tropical Andes. *Science*, *312*(5781), 1755–1756. doi: 10.1126/science.1128087

Bradley, R. S., Vuille, M., Hardy, D., & Thompson, L. G. (2003, 2). Low latitude ice cores record Pacific sea surface temperatures. *Geophysical Research Letters*, *30*(4), 2–5. doi: 10.1029/2002GL016546

Brantley, S. L., Kubicki, J. D., & White, A. F. (2008). Kinetics of water-rock interaction.

Brighenti, S., Tolotti, M., Bruno, M. C., Wharton, G., Pusch, M. T., & Bertoldi, W. (2019). Ecosystem shifts in alpine streams under glacier retreat and rock glacier thaw: A review. *The Science of the total environment*, *675*, 542–559.

Brown, G. H. (2002). Glacier meltwater hydrochemistry. *Applied Geochemistry*, *17*(7), 855–883.

Buytaert, W., & Beven, K. (2011, 5). Models as multiple working hypotheses: hydrological simulation of tropical alpine wetlands. *Hydrological Processes*, *25*(11), 1784–1799. doi: 10.1002/hyp.7936

Buytaert, W., Célleri, R., De Bièvre, B., Cisneros, F., Wyseure, G., Deckers, J., & Hofstede, R. (2006, 11). Human impact on the hydrology of the Andean páramos. *Earth-Science Reviews*, *79*(1-2), 53–72. doi: 10.1016/j.earscirev.2006.06.002

Clapperton, C. M. (1990, 1). Glacial and volcanic geomorphology of the Chimborazo-Carihuairazo Massif, Ecuadorian Andes. *Transactions of the Royal Society of Edinburgh: Earth Sciences*, *81*(02), 91–116. doi: 10.1017/S0263593300005174

Clow, D. W., & Mast, M. A. (2010). Mechanisms for chemostatic behavior in catchments: implications for co2 consumption by mineral weathering. *Chemical Geology*, *269*(1-2), 40–51.

Collins, D. N. (1999). Solute flux in meltwaters draining from a glacierized basin in the karakoram mountains. *Hydrological processes*, *13*(18), 3001–3015.

Devito, K., Creed, I., Gan, T., Mendoza, C., Petrone, R., Silins, U., & Smerdon, B. (2005). A framework for broad-scale classification of hydrologic response units on the boreal plain: Is topography the last thing to consider? *Hydrological Processes: An International Journal*, *19*(8), 1705–1714.

Ek, M. B., Mitchell, K. E., Lin, Y., Rogers, E., Grunmann, P., Koren, V., … Tarpley, J. D. (2003). Implementation of Noah land surface model advances in the National Centers for Environmental Prediction operational mesoscale Eta model. *Journal of Geophysical Research: Atmospheres*, *108*(D22).

Engel, M., Penna, D., Bertoldi, G., Dell'Agnese, A., Soulsby, C., & Comiti, F. (2016, 1). Identifying run-off contributions during melt-induced run-off events in a glacierized alpine catchment. *Hydrological Processes*, *30*(3), 343–364. doi: 10.1002/hyp.10577

Engel, M., Penna, D., Bertoldi, G., Vignoli, G., Tirler, W., & Comiti, F. (2019). Controls on spatial and temporal variability of streamflow and hydrochemistry in a glacierized catchment.

Farvolden, R. (1963). Geologic controls on ground-water storage and base flow. *Journal of hydrology*, *1*(3), 219–249.

Favier, V. (2004). Glaciers of the outer and inner tropics: A different behaviour but a common response to climatic forcing. *Geophysical Research Letters*, *31*(16), L16403. doi: 10.1029/2004GL020654

Feng, F., Li, Z., Jin, S., Dong, Z., & Wang, F. (2012). Hydrochemical characteristics and solute dynamics of meltwater runoff of urumqi glacier no. 1, eastern tianshan, northwest china. *Journal of Mountain Science*, *9*(4), 472–482.

Fortner, S. K., Mark, B. G., McKenzie, J. M., Bury, J., Trierweiler, A., Baraer, M., … Munk, L. (2011). Elevated stream trace and minor element concentrations in the foreland of receding tropical glaciers. *Applied Geochemistry*, *26*(11), 1792–1801.

Francou, B. (2004). New evidence for an ENSO impact on low-latitude glaciers: Antizana 15, Andes of Ecuador. *Journal of Geophysical Research*, *109*(D18), D18106. doi: 10.1029/2003JD004484

Gibss, R. (1967). The geochemistry of the amazon river system: Part 1. *The factors that control the salinity and the composition and concentration of the suspended solids. Geological Society of American Bulletin*, *78*, 1203–1232.

Godsey, S. E., Kirchner, J. W., & Clow, D. W. (2009). Concentration–discharge relationships reflect chemostatic characteristics of us catchments. *Hydrological Processes: An International Journal*, *23*(13), 1844–1864.

Godsey, S. E., Kirchner, J. W., & Tague, C. L. (2014). Effects of changes in winter snowpacks on summer low flows: Case studies in the Sierra Nevada, California, USA. *Hydrological Processes*, *28*(19), 5048–5064. doi: 10.1002/hyp.9943

Harrington, J. S., Mozil, A., Hayashi, M., & Bentley, L. R. (2018). Groundwater flow and storage processes in an inactive rock glacier. *Hydrological Processes*, *32*(20), 3070–3088.

Helgeson, H. C., Murphy, W. M., & Aagaard, P. (1984). Thermodynamic and kinetic constraints on reaction rates among minerals and aqueous solutions. ii. rate constants, effective surface area, and the hydrolysis of feldspar. *Geochimica et Cosmochimica Acta*, *48*(12), 2405–2432.

Hem, J. D. (1985). *Study and interpretation of the chemical characteristics of natural water* (Vol. 2254). Department of the Interior, US Geological Survey.

Herndon, E. M., Dere, A. L., Sullivan, P., Norris, D., Rynolds, B., & Brantley, S. L. (2015). Landscape heterogeneity drives contrasting concentration–discharge relationships in shale headwater catchments.

Hindshaw, R. S., Tipper, E. T., Reynolds, B. C., Lemarchand, E., Wiederhold, J. G., Magnusson, J., … Bourdon, B. (2011). Hydrological control of stream water chemistry in a glacial catchment (damma glacier, switzerland). *Chemical Geology*, *285*(1-4), 215–230.

Hood, J. L., Roy, J. W., & Hayashi, M. (2006). Importance of groundwater in the water balance of an alpine headwater lake. *Geophysical Research Letters*, *33*(13), 1–5. doi: 10.1029/

2006GL026611
Huth, A. K., Leydecker, A., Sickman, J. O., & Bales, R. C. (2004). A two-component hydrograph separation for three high-elevation catchments in the Sierra Nevada, California. *Hydrological Processes*, *18*(9), 1721–1733. doi: 10.1002/hyp.1414
INEC. (2010). Cencos de Poblacion y Vivienda 2010. *Quito, Ecuador*.
IPCC, C. C. (2007). Impacts, adaptation and vulnerability. contribution of working group ii to the fourth assessment report of the intergovernmental panel on climate change. *Intergovernmental Panel on Climate Change (IPCC), Cambridge University Press, New York*.
Johnson, N. M., Likens, G. E., Bormann, F., Fisher, D., & Pierce, R. (1969). A working model for the variation in stream water chemistry at the hubbard brook experimental forest, new hampshire. *Water Resources Research*, *5*(6), 1353–1363.
Kaser, G., Grosshauser, M., & Marzeion, B. (2010). Contribution potential of glaciers to water availability in different climate regimes. *Proceedings of the National Academy of Sciences*, *107*(47), 20223–20227. doi: 10.1073/pnas.1008162107
Kaser, G., & Osmaston, H. (2002). *Tropical glaciers*. Cambridge University Press.
Katsuyama, M., Tani, M., & Nishimoto, S. (2010). Connection between streamwater mean residence time and bedrock groundwater recharge/discharge dynamics in weathered granite catchments. *Hydrological Processes*, *24*(16), 2287–2299.
Kumar, N., Ramanathan, A., Tranter, M., Sharma, P., Pandey, M., Ranjan, P., & Raju, N. J. (2019). Switch in chemical weathering caused by the mass balance variability in a himalayan glacierized basin: a case of chhota shigri glacier. *Hydrological sciences journal*, *64*(2), 179–189.
La Frenierre, J., & Mark, B. G. (2014, 4). A review of methods for estimating the contribution of glacial meltwater to total watershed discharge. *Progress in Physical Geography*, *38*(2), 173–200. doi: 10.1177/0309133313516161
La Frenierre, J., & Mark, B. G. (2017). Detecting Patterns of Climate Change at Volcán Chimborazo, Ecuador, by Integrating Instrumental Data, Public Observations, and Glacier Change Analysis. *Annals of the American Association of Geographers*, *107*(4), 979–997. doi: 10.1080/24694452.2016.1270185
Lasaga, A. C. (1984). Chemical kinetics of water-rock interactions. *Journal of geophysical research: solid earth*, *89*(B6), 4009–4025.
Lewis, T., Lafrenière, M. J., & Lamoureux, S. F. (2012). Hydrochemical and sedimentary responses of paired high arctic watersheds to unusual climate and permafrost disturbance, cape bounty, melville island, canada. *Hydrological Processes*, *26*(13), 2003–2018.
Li, L., Bao, C., Sullivan, P. L., Brantley, S., Shi, Y., & Duffy, C. (2017). Understanding watershed hydrogeochemistry: 2. synchronized hydrological and geochemical processes drive stream chemostatic behavior. *Water Resources Research*, *53*(3), 2346–2367.
Maher, K. (2011). The role of fluid residence time and topographic scales in determining chemical fluxes from landscapes. *Earth and Planetary Science Letters*, *312*(1-2), 48–58.
Mark, B. G., French, A., Baraer, M., Carey, M., Bury, J., Young, K. R., … Lautz, L. (2017). Glacier loss and hydro-social risks in the Peruvian Andes. *Global and Planetary Change*, *159*(October), 61–76. doi: 10.1016/j.gloplacha.2017.10.003
Mark, B. G., & Mckenzie, J. M. (2007, 10). Tracing Increasing Tropical Andean Glacier Melt with Stable Isotopes in Water. *Environmental Science & Technology*, *41*(20), 6955–6960. doi: 10.1021/es071099d
Mayer, K. U., Frind, E. O., & Blowes, D. W. (2002). Multicomponent reactive transport modeling in variably saturated porous media using a generalized formulation for kinetically controlled reactions. *Water Resources Research*, *38*(9), 13–1.
McClain, M. E., & Naiman, R. J. (2008). Andean influences on the biogeochemistry and ecology of the amazon river. *BioScience*, *58*(4), 325–338.
McGuire, K., McDonnell, J. J., Weiler, M., Kendall, C., McGlynn, B., Welker, J., & Seibert, J. (2005). The role of topography on catchment-scale water residence time. *Water Resources Research*, *41*(5).
McLaughlin, R. (2017). *Hydrochemical Signatures of Glacial Meltwater on Volcán Chimborazo, Ecuador* (Unpublished doctoral dissertation).

Messerli, B., Viviroli, D., & Weingartner, R. (2004). Mountains of the World: Vulnerable Water Towers for the 21st Century. *Ambio*, 29–34.
Milner, A. M., Brown, L. E., & Hannah, D. M. (2009). Hydroecological response of river systems to shrinking glaciers. *Hydrological Processes: An International Journal*, *23*(1), 62–77.
Milner, A. M., Khamis, K., Battin, T. J., Brittain, J. E., Barrand, N. E., Füreder, L., … others (2017). Glacier shrinkage driving global changes in downstream systems. *Proceedings of the National Academy of Sciences*, *114*(37), 9770–9778.
Minaya, V. G., Maldonado. (2016). Ecohydrology of the Andes Páramo Region. *PhD diss., IHE Delft Institute for Water Education*.
Moriasi, D. N., Arnold, J. G., Van Liew, M. W., Bingner, R. L., Harmel, R. D., & Veith, T. L. (2007). Model evaluation guidelines for systematic quantification of accuracy in watershed simulations. *Transactions of the ASABE*, *50*(3), 885–900.
Nash, J., & Sutcliffe, J. (1970). River forecasting using conceptual models: Part 1-a discussion of principles. *Journal of Hydrology*, *10*(3), 280–290.
Ostheimer, G. J., Hadjivasiliou, H., Kloer, D. P., Barkan, A., & Matthews, B. W. (2005). Structural analysis of the group ii intron splicing factor crs2 yields insights into its protein and rna interaction surfaces. *Journal of molecular biology*, *345*(1), 51–68.
Pepin, N., Bradley, R. S., Diaz, H. F., Baraer, M., Caceres, E. B., Forsythe, N., … Yang, D. Q. (2015, 5). Elevation-dependent warming in mountain regions of the world. *Nature Climate Change*, *5*(5), 424–430. doi: 10.1038/nclimate2563
Podwojewski, P., Poulenard, J., Zambrana, T., & Hofstede, R. (2002). Overgrazing effects on vegetation cover and properties of volcanic ash soil in the pàramo of Llangahua and al Esperanza (Tungurahua, Ecuador). *Management*, *18*, 45–55. doi: 10.1079/SUM2001100
Pohl, E., Knoche, M., Gloaguen, R., Andermann, C., & Krause, P. (2015, 7). Sensitivity analysis and implications for surface processes from a hydrological modelling approach in the Gunt catchment, high Pamir Mountains. *Earth Surface Dynamics*, *3*(3), 333–362. doi: 10.5194/esurf-3-333-2015
Poppe, L., Paskevich, V., Hathaway, J., & Blackwood, D. (2001). A laboratory manual for x-ray powder diffraction. *US Geological Survey open-file report*, *1*(041), 1–88.
Qu, Y., & Duffy, C. J. (2007, 8). A semidiscrete finite volume formulation for multiprocess watershed simulation. *Water Resources Research*, *43*(8), 1–18. doi: 10.1029/2006WR005752
Saberi, L., McLaughlin, R. T., Crystal Ng, G., La Frenierre, J., Wickert, A. D., Baraer, M., … Mark, B. G. (2019). Multi-scale temporal variability in meltwater contributions in a tropical glacierized watershed. *Hydrology and Earth System Sciences*, *23*(1), 405–425.
Samaniego, P., Barba, D., Robin, C., Fornari, M., & Bernard, B. (2012, 4). Eruptive history of Chimborazo volcano (Ecuador): A large, ice-capped and hazardous compound volcano in the Northern Andes. *Journal of Volcanology and Geothermal Research*, *221-222*, 33–51. doi: 10.1016/j.jvolgeores.2012.01.014
Shanley, J. B., McDowell, W. H., & Stallard, R. F. (2011). Long-term patterns and short-term dynamics of stream solutes and suspended sediment in a rapidly weathering tropical watershed. *Water Resources Research*, *47*(7).
Shi, Y., Davis, K. J., Duffy, C. J., & Yu, X. (2013, 10). Development of a Coupled Land Surface Hydrologic Model and Evaluation at a Critical Zone Observatory. *Journal of Hydrometeorology*, *14*(5), 1401–1420. doi: 10.1175/JHM-D-12-0145.1
Shoji, S., Nanzyo, M., & Dahlgren, R. (1994). *Volcanic ash soils: genesis, properties and utilization*. Elsevier.
Sicart, J. E., Hock, R., & Six, D. (2008, 12). Glacier melt, air temperature, and energy balance in different climates: The Bolivian Tropics, the French Alps, and northern Sweden. *Journal of Geophysical Research*, *113*(D24), D24113. doi: 10.1029/2008JD010406
Smith, J. A., Mark, B. G., & Rodbell, D. T. (2008). The timing and magnitude of mountain glaciation in the tropical andes. *Journal of Quaternary Science: Published for the Quaternary Research Association*, *23*(6-7), 609–634.
Somers, L. D., McKenzie, J. M., Mark, B. G., Lagos, P., Ng, G.-H. C., Wickert, A. D., … Silva, Y. (2019). Groundwater buffers decreasing glacier melt in an andean watershedbut not forever. *Geophysical Research Letters*, *46*(22), 13016–13026.

Stachnik, Ł., Majchrowska, E., Yde, J. C., Nawrot, A. P., Cichała-Kamrowska, K., Ignatiuk, D., & Piechota, A. (2016). Chemical denudation and the role of sulfide oxidation at werenskioldbreen, svalbard. *Journal of Hydrology*, *538*, 177–193.

Stallard, & Edmond. (1983). Geochemistry of the amazon: 2. the influence of geology and weathering environment on the dissolved load. *Journal of Geophysical Research: Oceans*, *88*(C14), 9671–9688.

Stallard, R. F., & Murphy, S. F. (2014). A unified assessment of hydrologic and biogeochemical responses in research watersheds in eastern puerto rico using runoff–concentration relations. *Aquatic geochemistry*, *20*(2-3), 115–139.

Stern, C. R. (2004). Active andean volcanism: its geologic and tectonic setting. *Revista geológica de Chile*, *31*(2), 161–206.

Tague, C., Grant, G., Farrell, M., Choate, J., & Jefferson, A. (2008, 1). Deep groundwater mediates streamflow response to climate warming in the Oregon Cascades. *Climatic Change*, *86*(1-2), 189–210. doi: 10.1007/s10584-007-9294-8

Takahashi, T., & Shoji, S. (2002). Distribution and classification of volcanic ash soils. *GLOBAL ENVIRONMENTAL RESEARCH-ENGLISH EDITION-*, *6*(2), 83–98.

Tetzlaff, D., Seibert, J., McGuire, K., Laudon, H., Burns, D. A., Dunn, S., & Soulsby, C. (2009). How does landscape structure influence catchment transit time across different geomorphic provinces? *Hydrological Processes: An International Journal*, *23*(6), 945–953.

Torres, M. A., Moosdorf, N., Hartmann, J., Adkins, J. F., & West, A. J. (2017). Glacial weathering, sulfide oxidation, and global carbon cycle feedbacks. *Proceedings of the National Academy of Sciences*, *114*(33), 8716–8721.

Torres, M. A., West, A. J., & Clark, K. E. (2015). Geomorphic regime modulates hydrologic control of chemical weathering in the andes–amazon. *Geochimica et Cosmochimica Acta*, *166*, 105–128.

Tranter, M., Brown, G. H., Hodson, A. J., & Gurnell, A. M. (1996). Hydrochemistry as an indicator of subglacial drainage system structure: a comparison of alpine and sub-polar environments. *Hydrological Processes*, *10*(4), 541–556.

Ugolini, F. C., Dahlgren, R. A., et al. (2002). Soil development in volcanic ash. *GLOBAL ENVIRONMENTAL RESEARCH-ENGLISH EDITION-*, *6*(2), 69–82.

Veettil, B. K., Leandro Bayer Maier, E., Bremer, U. F., & de Souza, S. F. (2014, 12). Combined influence of PDO and ENSO on northern Andean glaciers: a case study on the Cotopaxi ice-covered volcano, Ecuador. *Climate Dynamics*, *43*(12), 3439–3448. doi: 10.1007/s00382-014-2114-8

Vermote, E. (2015). MOD09A1 MODIS/Terra Surface Reflectance 8-Day L3 Global 500m SIN Grid V006. *NASA EOSDIS Land Processes DAAC*.

Vuille, M., & Bradley, R. S. (2000). the tropical Andes. *Geophysical Research Letters*, *27*(23), 3885–3888.

Vuille, M., Francou, B., Wagnon, P., Juen, I., Kaser, G., Mark, B. G., & Bradley, R. S. (2008, 8). Climate change and tropical Andean glaciers: Past, present and future. *Earth-Science Reviews*, *89*(3-4), 79–96. doi: 10.1016/j.earscirev.2008.04.002

Vuille, M., & Keimig, F. (2004, 9). Interannual Variability of Summertime Convective Cloudiness and Precipitation in the Central Andes Derived from ISCCP-B3 Data. *Journal of Climate*, *17*(17), 3334–3348. doi: 10.1175/1520-0442(2004)017<3334:IVOSCC>2.0.CO;2

Wagnon, P., Ribstein, P., Francou, B., & Sicart, J. E. (2001). Anomalous heat and mass budget of Glaciar Zongo , Bolivia , during the 1997 / 98 El Ni · o year. *Journal of Glaciology*, *47*(156), 21–28.

Wen, H., Perdrial, J., Bernal, S., Abbott, B. W., Dupas, R., Godsey, S. E., … others (2020). Temperature controls production but hydrology controls export of dissolved organic carbon at the catchment scale.

White, A. F., Blum, A. E., Schulz, M. S., Vivit, D. V., Stonestrom, D. A., Larsen, M., … Eberl, D. (1998). Chemical weathering in a tropical watershed, luquillo mountains, puerto rico: I. long-term versus short-term weathering fluxes. *Geochimica et Cosmochimica Acta*, *62*(2), 209–226.

Williams, M. W., Hood, E., Molotch, N. P., Caine, N., Cowie, R., & Liu, F. (2015). The teflon basinmyth: hydrology and hydrochemistry of a seasonally snow-covered catchment. *Plant Ecology & Diversity*, *8*(5-6), 639–661.

Wilson, A. M., Williams, M. W., Kayastha, R. B., & Racoviteanu, A. (2016, 3). Use of a hydrologic mixing model to examine the roles of meltwater, precipitation and groundwater in the Langtang River basin, Nepal. *Annals of Glaciology*, *57*(71), 155–168. doi: 10.3189/2016AoG71A067

Wolery, T. J. (1992). Eq3/6, a software package for geochemical modeling of aqueous systems: package overview and installation guide (version 7.0).

Zhi, W., Li, L., Dong, W., Brown, W., Kaye, J., Steefel, C., & Williams, K. H. (2019). Distinct source water chemistry shapes contrasting concentration-discharge patterns. *Water Resources Research*, *55*(5), 4233–4251.

Supplemental Materials: Spatiotemporal Drivers of Hydrochemical Variability in a Tropical Glacierized Watershed in the Ande

1 Uncertainty Analysis

Perturbed horizontal hydraulic conductivity (KSATH), vertical hydraulic conductivity (KSATV), porosity, and van Genuchten water retention curve parameters were implemented in the model to produce uncertainty distributions for stream discharge, groundwater chemistry, and stream chemistry. Initially the model was manually calibrated to obtain a narrow range of potential values for each parameter. An upper and lower bound was assigned to each parameter to span the range of possible values based on calibration results and values reported in literature (Table S1).

	Parameter	Range assigned (Literature values)	Notes and References
Horizontal hydraulic conductivity	1.1E-07 to 9.5E-07 ((2.5E-08 to 2.5E-06))	Unconsolidated glacial and fluvial sediments (Dominico and Shwartz, 1990)	
Vertical hydraulic conductivity	3E-08 to 7E-07 (5.5E-08 to 5.5E-06)	Anisotropy=2	
Posority	0.1 to 0.55 (0.1-0.3) (0.3-0.65)	Unconsolidated sediments Fractured bedrock (Earle S., 2018)	
Alpha	0.1 to 0.5 (0.01 to 0.7)	Unconsolidated sediments (Porebska et al., 2006)	
Beta	1 to 2.5 (1 to 3.6)	Unconsolidated sediments (Porebska et al., 2006)	

Table S1: Select parameters perturbed for the ensemble run, the range of values based on literature in parentheses, and the range of values assigned.

Latin hypercube sampling method was used to randomly sample parameters from uniform distributions for each parameter, and the model was run for 20 random sets of parameters. The ensemble of 20 model runs with perturbed soil hydraulic properties, including saturated horizontal hydraulic conductivity (KSATH), saturated vertical hydraulic conductivity (KSATV), porosity, and Van-Genuchten water retention curve parameters, is shown in figure S-1 in gray lines. The calibrated simulation of stream concentrations at the outlet are represented in red lines, which match reasonably well with measured concentrations in the stream during the 2015 and 2016 field campaigns.

Major ion concentrations also reasonably match observed concentrations at different sampling points along the stream. The simulated Na+ concentrations at SW-1, SW-2, and SW-3 sampling points (Figure 2a) are shown in Figure S2.

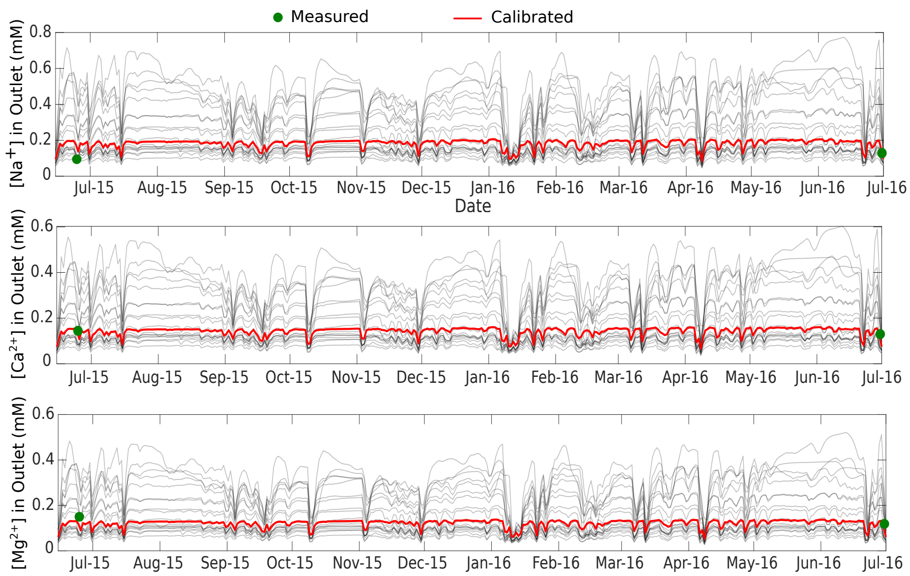

Figure S1: Calibrated simulations of stream concentrations for Na^+, Ca^{2+}, and Mg^{2+} at the outlet, shown in red lines, compared to the measured stream concentrations at the SW-4 site (Figure 2a). Gray lines show the ensemble of simulated concentrations at the outlet with a range of soil hydraulic properties.

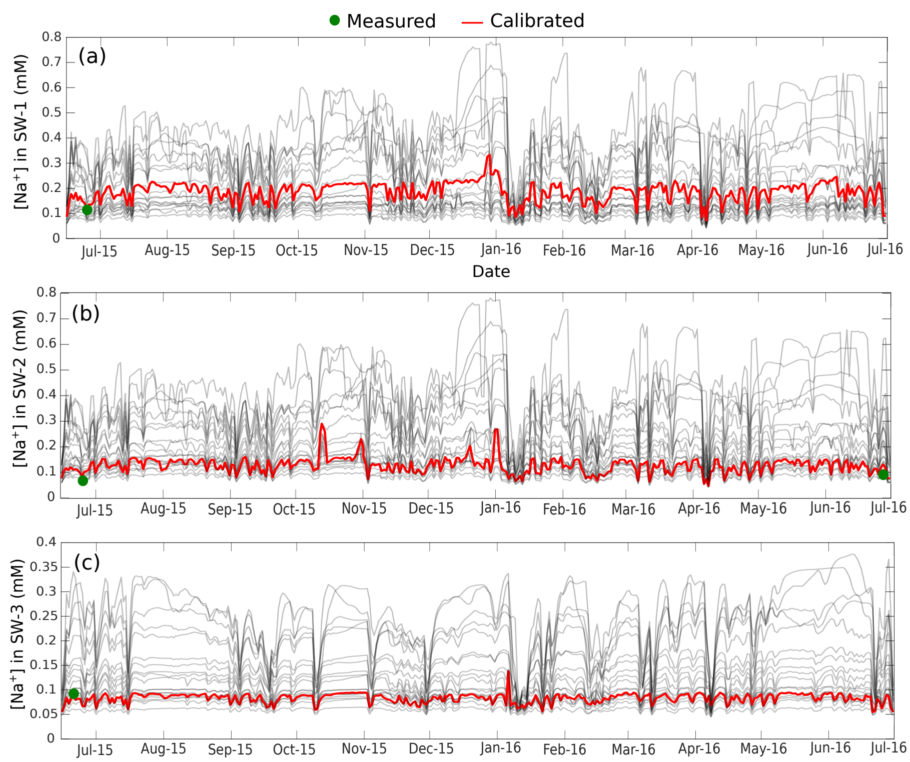

Figure S2: Simulated and measured Na^+ concentrations in a) sampling site SW-1, b) sampling site SW-2, and c) sampling site SW-3

2 Clibrated Parameters

Table S2 shows the calibrated parameters with and without hydrochemical constraints.

	KINFV (m/s)		KSATV (m/s)		KSATH (m/s)		Porosity		α (1/m)		β (-)	
Ice-covered	2.07E-7	1.64E-7	4.56E-8	5.36E-8	6.71E-7	7.56E-7	0.461	0.296	0.863	0.412	1.06	1.038
Sparsely Vegetated	1.43E-7	1.74E-7	4.63E-8	4.85E-8	4.63E-7	5.85E-7	0.459	0.296	0.585	0.437	1.063	1.038
Grassland	1.23E-7	1.87E-7	4.02E-8	5.27E-8	4.02E-7	5.27E-7	0.493	0.297	0.488	0.469	1.066	1.039

Table S2: Calibrated parameters without (Saberi et al., 2019) and with hydrochemical constraints. Parameters include hydraulic conductivities for vertical infiltration (KINFV), vertical saturated flow (KSATV), horizontal saturated flow (KSATH), porosity, residual soil moisture, and shape parameters (α and β) for the Van Genuchten moisture retention curve: $\theta = \theta_{res} + porosity \times \left(\frac{1}{1+|\alpha\psi|^{\beta}}\right)^{(1-\frac{1}{\beta})}$, with water content θ and pressure head ψ.

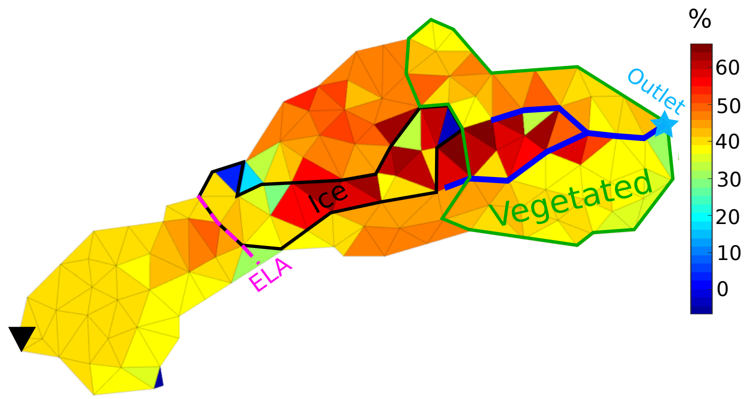

Figure S3: Percent change in the Na+ concentrations in groundwater by mineral dissolution over the entire watershed. The black triangle shows the peak of Volcan Chimborazo (6280 m a.s.l.). The dashed pink line represents the ELA at 5050 m a.s.l. The black outline indicates the glacierized grid cells below the ELA, in which glacier melt is applied in model. The green outline identifies the vegetated part of the watershed. The blue line shows the stream line and the blue star represents the outlet. Vegetated areas are shown in Figure 2a.